Cathodic activation of synthesized highly defective monoclinic hydroxyl-functionalized ZrO_2 nanoparticles for efficient electrochemical production of hydrogen in alkaline Media

Nasser Y. Mostafa[1,2] | Mohsen M. Qhtani[1] | Saad H. Alotaibi[3] | Zaki I.Zaki[1,4] | Sarah Alharthi[1] | Mateusz Cieslik[5] | Karolina Gornicka[6] | Jacek Ryl[5] | Rabah Boukherroub[7] | Mohammed A. Amin*[1,8]

[1]Materials Science and Engineering Group, Department of Chemistry, Faculty of Science, Taif University, 888 Hawaiya, Saudi Arabia

[2]Department of Chemistry, Faculty of Science, Suez Canal University, Ismailia, Egypt

[3]Department of Chemistry, Faculty of Turabah University College, Taif University, Turabah 21995, Saudi Arabia

[4]Advanced Materials Department, Central Metallurgical Research and Development Institute, Cairo, Egypt

[5]Department of Electrochemistry, Corrosion and Materials Engineering, Faculty of Chemistry, Gdansk University of Technology, Narutowicza 11/12, 80-233 Gdansk, Poland

[6]Department of Solid-State Physics, Faculty of Applied Physics and Mathematics, Gdansk University of Technology, Narutowicza 11/12, 80-233 Gdansk, Poland

[7]Univ. Lille, CNRS, Central Lille, Univ. Polytechnique Hauts-de-France, UMR 8520, IEMN, F-59000 Lille, France

[8]Department of Chemistry, Faculty of Science, Ain Shams University, 11566 Abbassia, Cairo, Egypt

Summary

The high electrochemical stability of Zirconia (ZrO_2) at high potentials strongly suggested it as an alternative to carbon supports which experience reduced efficiency due to some corrosion problems particularly during prolonged electrocatalysis activity. However, the use of ZrO_2 was limited by its low electrical conductivity and surface area. In this work, we developed a methodology for synthesizing monoclinic ZrO_2 NPs with increased surface area and improved electrical/electrocatalytic characteristics without using any carbon-based co-support material or any metallic nanoparticles. In this context, for the first time highly defective hydroxyl-functionalized ZrO_2 NPs (designated here as ZT NPs) were prepared by a hydrothermal route in the presence of sodium tartrate as a mineralizer. XRD demonstrated that the produced zirconia was semi-crystalline microspheres, consisting of monoclinic ZrO_2 NPs with high lattice defects. The addition of tartrate ions decreased the crystallite size and increased the defects and microstrain. At the same time, the alkaline hydrogen evolution reaction (HER) catalytic activity of ZrO_2 NPs was significantly increased when using sodium tartrate as mineralizer; the overpotential required to obtain 10 mA cm^{-2} (η_{10}) dropped down from 490 to merely 235 mV, while an exchange current density (j_o) increased 12 times to 0.22 mA cm^{-2}. The presence of structure defects (revealed by XRD) and the increased number of active surface sites contending O-H groups (evidenced from ATR-FTIR and XPS) as well as the enhanced electrochemical active surface area (confirmed from double-layer capacitance measurements) were the main reasons behind the high catalytic performance**.** The ZrO_2 NPs catalytic activity increased even further during the long-term stability tests under severe cathodic conditions (ZT*, ZrO_2 NPs obtained after the long-term stability, has j_o = 0.47 mA cm^{-2} and η_{10} = 140 mV), approaching the activity of Pt/C catalyst. This process was assisted by mineralizer removal from the catalyst (testified by XPS). Our studies revealed that ZT* are characterized by larger electroactive

surface area and more structure defects compared to ZT, where surface area and microstrains resulting from surface hydroxylation open cavities in zirconia structure.

KEYWORDS

Defective monoclinic ZrO_2; Hydrothermal synthesis; Electrocatalysis; Hydrogen evolution reaction.

1 | INTRODUCTION

One of the fundamental processes in electrocatalysis is the hydrogen evolution reaction (HER), which plays a vital role in energy conversion devices.[1] The HER is traditionally depicted by the concatenation of three elementary steps.[2] Hydrogen intermediates (H_{ads}) are initially formed *via* the Volmer step, which involves, depending on solution pH, protons discharge, Eq. (1), or water, Eq. (2).

$$H^+ + e^- \leftrightarrow H_{ads} \quad (1)$$

$$H_2O + e^- \leftrightarrow H_{ads} + OH^- \quad (2)$$

The Volmer step is either followed by the Tafel reaction (chemical desorption, Eq. (3)) or Heyrovsky step, electrochemical desorption: Eq. (4) (low pH) or Eq. (5) (high pH).

$$2H_{ads} \leftrightarrow H_2 \quad (3)$$

$$H^+ + H_{ads} + e^- \leftrightarrow H_2 \quad (4)$$

$$H_2O + H_{ads} + e^- \leftrightarrow H_2 + OH^- \quad (5)$$

Numerous publications reported that the HER on a wide range of electrocatalysts is pH-dependent, generally decreases with increasing pH.[3-5] Experimental findings revealed that the kinetics (expressed in exchange current density, j_o) of the HER in alkaline media is lower than that in acidic ones by 2-3 orders of magnitude.[6-9] Even on Pt, the most promising and highly efficient electrocatalyst for the HER, owing to its high reactivity for the adsorption and recombination of reactive hydrogen intermediates,[10] the HER exhibited slower kinetics in alkaline solutions, as compared to acidic ones.[11] The reduced efficacy of the water dissociation step on the Pt surface, Eq. (6), which constitutes an additional

energy barrier to the kinetics of the overall reaction rate, is the main reason behind the sluggish kinetics of the alkaline HER on Pt surface.[12]

$$H_2O + Pt + e^- \rightarrow Pt{-}H + OH^- \quad (6)$$

High overpotential (referring to high energy consumption) is, therefore, needed to enhance the indolent kinetics of the HER in an alkaline medium. This diminished HER rate in alkaline solutions has retarded advances in high-purity hydrogen generation techniques, such as water splitting.[12-14] So far, high-surface-area Raney Ni and Ni alloys,[15-17] and many others[12-14] are used as active electrocatalysts for alkaline HER and in the conventional alkaline water electrolyzers. Although most of these materials are cost-effective, they are not efficient enough to generate large amounts of hydrogen at low overpotentials so as to replace Pt-based electrocatalysts in energy conversion devices. This made the development of highly efficient, non-precious, and stable electrocatalysts to produce hydrogen from alkaline solutions a major challenge.[12-14] For instance, R. Solmaz group fabricated 3D Cu[18], Ag[19], and Ni[20] nanodomes as efficient electrocatalysts for the HER and water splitting in alkaline solutions. In another study, the same group synthesized Mo-modified carbon felt (CF)[21] MoPd//CF/Mo[22], and Au/activated NiZn coatings[23] electrodes and reported them as effective cathodes for the alkaline hydrogen generation. Recently, in our lab, highly stable Eu_2O_3/TiO_2, PdO/TiO_2, and ZnO/TiO_2 nanocomposites have been synthesized and demonstrated as highly active electrocatalysts for the HER in alkaline electrolytes.[24,25] In very recent studies, nanostructured Gd-In-Zn ternary oxide and anionic NiS_2-$Ni(OH)_2$ nanosheets/nickel foam were reported as efficacious electrocatalysts for alkaline overall water splitting and HER.[26,27]

Zirconia (ZrO_2) has many advisable physicochemical characteristics that are technologically important. These include outstanding mechanical properties, exceptional thermal stability, increased corrosion resistance, and good chemical stability and thus, has been commonly used in many applications.[28] ZrO_2 is considered as the best known material used for thermal barrier coating when doped with Y_2O_3(YSZ) due to its low mechanical resistance and thermal conductivity.[29] Monoclinic, cubic, and

tetragonal are the three major forms of crystalline zirconia. While the former form is stable below 1170°C, the later one is stable within a range of temperature of 1170-2370 °C. Above 2370 °C, the cubic form is stable.[30]

Current synthetic methods for industrial production of YSZ are conventional solid-state ceramic method or spray drying. Generally, the produced powders are in the microscale range.[31] Several methods were employed to yield nanosized YSZ powder. These comprise sol–gel,[32] co-precipitation[33] and hydrothermal routes.[34-37] One of the inclusively used methods for the production of various oxide nanostructures is the hydrothermal method.[38-41] In recent years, hydrothermal processing at an industrial scale has been revived. The central advantage of this processing route is that, the shape, size, crystallinity, and homogeneity of the produced powders can be controlled by regulating the reaction conditions such as temperature, time, solvent, surfactant and precursor characteristics.[39,42]

Owing to its high electrochemical stability at high potentials, ZrO_2 has been suggested as an alternative to carbon supports.[43] However, its use was limited by its low electrical conductivity. Hence new strategies need to be established to overcome the poor electrical conductivity and/or surface area of ZrO_2. Hybridization with or supporting on different materials, such as carbon-based materials, represents an appealing strategy to improve the electrical conductivity and surface area, and thus enhance the catalytic performance of ZrO_2-based materials.[44,45] For instance, Pt_4ZrO_2/C electrocatalyst, based on the work of Liu *et al.*, not only improved the efficiency of high temperature fuel cells, but also exhibited higher stability than the commercial Pt/C electrocatalyst.[46]

In another study, Bai *et al.* investigated the effect of Pt:ZrO_2 molar ratio on the catalytic activity of Pt – ZrO_2/C electrocatalyst towards the alkaline oxidation of methanol, and found that the Pt(1):ZrO_2(4) molar ratio achieved the highest catalytic performance, which is higher than that recorded by Pt/C.[47] Likewise, Cheng et al., revealed that Pt–ZrO_2/C exhibited very high stability and activity

towards oxygen reduction reaction (ORR), nine times more than that of Pt/C.[48] However, the presence of carbon materials as a co-support limits the industrial applications of these efficient electrocatalysts due to carbon corrosion followed by metal nanoparticles' agglomeration and dissolution.[47,48] In an attempt to overcome such issue, Aguilar-Vallejo *et al.* conquered this issue by synthesizing Pt electrocatalysts directly on ZrO_2 supports without using any carbon support.[49]

In this work, in order to evade the above mentioned drawbacks, we developed a methodology for synthesizing monoclinic ZrO_2 NPs with increased surface area and improved electrical/electrocatalytic characteristics without using any carbon-based co-support material or any metallic nanoparticles that may agglomerate and/or detach the support surface causing depression in efficiency. In this context, we prepared highly defective hydroxyl-functionalized ZrO_2 NPs by a hydrothermal route in the presence of sodium tartrate (for the first time) as a mineralizer. Being highly defective and conductive, the obtained ZrO_2 NPs were directly used here (for the first time) as an efficient electrocatalyst, and not as a supporting material as reported in the literature, for H_2 production in alkaline electrolytes. Our work's novelty is also evidenced from the literature which revealed no reports concerning the usage of bare ZrO_2 NPs as efficient electrocatalyst for the HER in alkaline solutions. In our very recent study[50], we synthesized ZrO_2 NPs with different defect densities using various sodium carboxylate salts. ZrO_2 NPs with the highest defects was obtained in presence of Na-tartrate, the carboxylate salt adopted here. In addition to defects, the ZrO_2 NPs synthesized in presence of tartrate ions exhibited a high degree of hydroxylation (Zr-O-H), which generally enhances the catalytic properties of the material.[51] The electrocatalytic activity of the resulting highly defective monoclinic hydroxyl-functionalized ZrO_2 NPs (named as ZT) was assessed for the HER in alkaline media. To clarify the catalytic impact of Na-tartrate salt, the ZT electrocatalytic activity was compared with that of ZrO_2 NPs prepared without Na-tartrate under the same hydrothermal conditions. Catalyst's stability was tested using repetitive cyclic cathodic polarization (10,000 cycles) measurements,

and the results revealed that not only does the catalyst retain its high performance after the 10,000th sweep cycle, but it is also activated yielding an activated catalyst (designated here as ZT*). During chronoamperometry measurements, performed at a fixed overpotential of -1.0 V *vs.* RHE for 72 h, the activation of the catalyst was also observed. Surface characterizations and HER electrocatalytic activity of the ZT* catalyst were also studied and discussed. Also presented here is a comparison between the activity and durability of the ZT and ZT* catalysts versus highly effective HER electrocatalysts published in the literature in alkaline media.

2 | EXPERIMENTAL

2.1 | Materials

All materials employed were analytical reagents, and their solutions were prepared using double distilled water. In 200 mL of doubly distilled water a mixture of zirconium oxychloride ($ZrOCl_2.8H_2O$) and sodium tartrate was dissolved in 1:0.5 molar ratio. The mixture was moved into a high-pressure autoclave Teflon-lined 300 mL and was heated for 24 h at 240 ^oC. The reaction was stirred at 350 rpm. The hydrothermal setup is displayed in Figure S1 (Supporting Information, Section S1).The ZrO_2 nanoparticles were separated through centrifugation at 6000 rpm for 30 min, washed 2 times with water then centrifuged again at 6000 rpm. The powder was dried at 105 ^oC for 24 h, then fully characterized employing XRD, SEM/EDX, XPS, HRTEM, and FTIR (Supporting Information, Section S2).

2.2 | Electrochemical measurements

Electrochemical measurements were conducted in 1.0 M KOH electrolyte using a standard double-jacketed three electrodes electrochemical cell. Various electrochemical techniques were applied to

evaluate HER electrocatalytic activity and stability of the tested materials, as fully reported in Section S3 (Supporting Information).

3 | RESULTS AND DISCUSSION

3.1 | Characterization of the synthesized catalysts

3.1.1 | XRD studies

The XRD patterns recorded for Z (ZrO_2 NPs synthesized without sodium tartrate) and ZT (ZrO_2 NPs synthesized in presence of sodium tartrate) powders are depicted in Figure 1. The results of the search match analysis of X'pert High Score manifested the existence of a monoclinical ZrO_2 phase (*P21/c*), card # 00-001-0750. The obvious peak broadening in the two patterns indicates the synthesized powders' nanocrystalline nature. Compared to Z sample, the ZT sample showed weaker and broader peaks, reflecting its semi-crystalline nature.

Using a modified Williamson-Hall (W-H) method, namely the Uniform Deformation Model (UDM) the lattice strain (ε) and crystallite size (D) were estimated from XRD data.[52] In that model, the strain is supposed to be uniform in all crystallographic directions, taking into account the crystal's isotropic nature. Figure S2 (Supporting Information) shows the Williamson-Hall plots of $\beta\cos(\theta)$ against $4\sin(\theta)$ for Z and ZT samples. In the case of ZT sample, the strain measured from the slope is found to increase significantly. Table S1 (Supporting Information) lists the estimated mean crystallite size and lattice strain of the two ZrO_2 samples. The presence of tartrate decreased the crystallite size from 19.5 to 12.8 nm, while the average maximum microstrain increased from 3.1×10^{-3} to 17.6×10^{-3}. The tartrate ions coordinated to Zr^{4+} during the synthesis may give rise to defects in the host lattice. Such defects are expected to cause distortion of the lattice and internal strains thus, impeding crystal growth.

3.1.2 | HRTEM examination

The HRTEM images depicted in Figure 2 describe samples' morphology and microstructure. It is obvious from image (a) that the Z sample's nanostructure morphology appears like rice kernels with varying aspect ratios. This manifests the anisotropic nature of the nanocrystals making up the monoclinical rode-like nanostructures of ZrO_2. The lattice's continuous parallel fringes, image (b), demonstrate that the monoclinic nanostructures of the ZrO_2 NPs are formed by slow-oriented nanocrystal growth and signalize high crystallinity. Figure 2(b) depicts a resolved lattice fringes pattern, indicating a single-crystalline-like phase and good crystallinity of the synthesized material. Any two successive fringes space at a distance of 0.315 nm. This distance is in consistence with the Muller index of the (111) monoclinic ZrO_2 planes thereby, conforming to the XRD analysis (Figure 1).

In contrast, the presence of sodium tartrate produced semi-crystalline microspheres (average diameter of 105 nm) consisting of ZrO_2 NPs, image (c). Displayed on ZT sample's HRTEM, image (d), are a few clear disordered lattice fringes, marked by white circles. This proposes high density of defects in the lattice, as formerly evidenced in XRD (Figure 1).

3.1.3 | ATR-FTIR spectroscopy measurements

Figure 3 displays the ATR-FTIR spectra of the pure monoclinic ZrO_2 samples. The broad band observed between 3580 and 3190 cm^{-1} is assigned to the stretching vibrations of adsorbed water molecules and surface O-H groups.[50] The well-defined bands at 1700-1500 cm^{-1} and 1322 cm^{-1} are ascribed to the vibration modes of the hydroxyl groups on the surface of the Z sample. The vibration band at 1632 cm^{-1} is allocated to the bending mode of adsorbed water. In the case of the ZT sample (which is generated in the presence of sodium tartrate) this band appears broader, most probably due to the presence of different

adsorbed states of water. The stretching bands at 1442 and 1322 $cm^{-1}$are due to the O-H surface groups,[53] and their intensities are more prominent in sample ZT (see the insert of Figure 3). It is recognized that zirconia with monoclinic structure, which is also known as mineral Baddeleyite, has extensive catalytic applications as its surface is heavily covered by hydroxyl groups.[54] The O-H groups in the monoclinic surface of the zirconia are located at two sites: terminal O-H groups (O-H coordinated to one Zr ion) and multi-coordinated O-H groups (O-H coordinated to two or three Zr ions).[54]

Additional peaks observed within the 450-830 cm^{-1} frequency range and are due to Zr-O.[55,56] The Z sample FTIR spectrum comprises well-resolved peaks in this region, confirming the highly crystalline nature of monoclinic ZrO_2. Such two peaks appear less resolved in the case of the ZT sample due to the microstrain and defects of the lattice. The vibration bandat 733 cm^{-1} is assigned to ZrO_4^+ tetrahedral vibration modes. The 665 and 563 cm^{-1} bands are allocated to the Zr-O-Zr and Zr-O vibrations, respectively.[53] The last two bands (563 and 655 cm^{-1}) characterize the monoclinic ZrO_2 phase.[57]

3.1.4 | SEM/EDS analysis

The EDS spectra of Z and ZT samples are displayed in Figure S3 (Supporting Information), revealing the presence of zirconium, oxygen and carbon elements. The atomic percentage (at%) of each element is shown in Table S2. The Zr:O ratio for the Z sample is 0.50:1 and 0.49:1 for the ZT sample, which is in very good agreement with ZrO_2 stoichiometry. The SEM micrographs of the analyzed powder agglomerates are presented in the inset of Figure S3.

3.1.5 | XPS studies

The XPS survey spectra (Figure 4A) revealed the presence of zirconium, oxygen and carbon elements within the analyzed samples. The recorded core level spectrum of the Zr_{2p}, Figure 4(B), was broad, revealing two different chemical states, which according to the literature and the XRD data were defined

as ZrO_2 with a different lattice structure. The dominant component, peaking at 181.6 eV, was ascribed to ZrO_2 with monoclinic structure, while the second, smaller component, red-shifted by +1.1 eV was defined as tetragonal ZrO_2.[58,59] It should also be noted that a very similar spectral shift is typically found for $Zr(OH)_4$, which was confirmed in large amounts using ATR-FTIR studies; therefore, the peak recorded at 182.7 eV for ZT catalyst should rather be featured as $Zr(OH)_4$,[60] as the XRD revealed no tetragonal structure within these nanoparticles.

Furthermore, as shown in Figure 4(C), the O_{1s} profile is overall quite complicated. The major two peaks, located at 529.5 and 530.5 eV were deconvoluted as ZrO_2 in monoclinic and $Zr(OH)_4$, respectively.[58,61] The third, broad O_{1s} component, peaking at approx. 531.4 eV is the most complex to explain, as it may have multiple equally-valuable origins; it could partially result from C-O bonds present in tartrate species used as mineralizer,[62] or from adventitious carbon contamination from air exposure and CO_2 adsorption. Also, the component couldpartially be related to water chemisorption and formation of surface hydroxide species $Zr(OH)_4$.[63] The analyzed C_{1s} peak can be curve-fitted with three components at 284.6, 286.5 and 288.6 eV ascribed to adventitious carbon and tartrate species.[62,64]

The analysis was summarized in Table 1. According to the high-resolution XPS analyses carried out in the O_{1s} and Zr_{2p} spectral range, the total Zr:O ratio ranges between 0.48:1 to 0.54:1, to be expected for ZrO_2 stoichiometry, with a low share of other valence states of zirconium. At the same time, the strength of O_{1s} peak at 531.4 eV, primarily associated with air atmosphere contamination, tartrate species and chemisorbed water species, is nearly twice as strong for ZT in comparison to Z catalyst.

3.2 | Electrocatalytic studies for the HER

3.2.1 | Cathodic polarization measurements

Figure 5(a) depicts the LSV curves recorded for Z and ZT catalysts in comparison with bare GC and commercial Pt/C electrodes. The various electrochemical parameters used to describe the kinetics of the HER were derived from Figure 5(b), constructed *via* fitting the linear polarization data of Figure 5(a) to the equation of Tafel. Table 2 summarizes such parameters for each tested catalyst.

There is an obvious shift in the onset potential (E_{HER}), the potential beyond which the cathodic current is steeply increased, towards more anodic (active) direction from bare GCE to Z and ZT catalysts. The E_{HER} value of the ZT sample that has been subjected to repetitive cyclic cathodic polarization (10,000 cycles) approached that of the Pt/C catalyst. This process of cathodic activation yielded an activated ZT catalyst, namely ZT* catalyst. In addition, the ZT catalyst's cathodic current beyond E_{HER} is steeper than that of Z. This steepness means that high cathodic currents (corresponding to large amount of H_2) can be generated at low cathodic potentials. For instance, an overpotential value of η_{10} = 235 mV was sufficient for ZT catalystto generate a current density of 10 mA cm^{-2}. This value further decreased to 140 mV, close to that measured for the Pt/C catalyst (η_{10} = 128 mV), upon cathodic activation (i.e., for ZT* catalyst).

On the other hand, Z catalyst required much higher overpotential (η_{10} = 490 mV) to deliver the same cathodic current. These findings reveal the high HER catalytic performance of ZT catalyst, which is further enhanced after cathodic activation to approach that of the state-of-the-art Pt/C catalyst. The promising HER catalytic activity of ZT* catalyst will be discussed later in section 3.2.4, where ZT catalyst was activated during long-term stability tests.

The steepness of the cathodic currents of ZT catalysts (inactivated ZT and activated, ZT*) is translated into higher exchange current density (j_o) values (0.22 and 0.47 mA cm^{-2} for ZT and

ZT* catalysts, respectively). The latter j_o value (0.47 mA cm^{-2}), which is 26 times greater than that recorded for Z catalyst (0.018 mA cm^{-2}), approached that of Pt/C (0.66 mA cm^{-2}). The mechanism of the HER in alkaline media proceeds in two steps,[17,65] namely Vomer (Eq. (7)), followed by either Heyrovsky, Eq. (8), or Tafel, Eq. (9):

$$H_2O + S^* + e^- \rightarrow S^*\text{-}H_{ads} + OH^- \quad (7)$$

$$H_2O + S^*\text{-}H_{ads} + e^- \rightarrow H_2 + S^* + OH^- \quad (8)$$

$$S^*\text{-}H_{ads} + S^*\text{-}H_{ads} \rightarrow S^* + S^* + H_2 \quad (9)$$

Where S^* and S^*-H_{ads} denote an active catalytic site on the catalyst surface and a hydrogen intermediate adsorbed on that active site, respectively. Based on the electrochemical results (Figure 5) and their associated HER kinetic parameters (Table 2) discussed above, it is plausible to conclude that the active catalytic sites (catalyst surface's defects and –OH functional groups) on the ZT surface markedly accelerated the kinetics of water reduction in the Volmer step.

The HER rate-determining step can be deduced from Tafel slope. Butler-Volmer kinetics revealed 120, 40, or 30 mV dec^{-1} numerical values for Tafel slope (β_c) when the Volmer, Heyrovsky, or Tafel step is the rate-determining step, respectively.[13,66] β_c values of 125 and 122 mV dec^{-1} were calculated for ZT and ZT* catalysts, respectively. These values are near to the ideal value for the Volmer step (120 mV dec^{-1}), suggesting this step as the rate-limiting ofthe HER on ZT and ZT*. However, a Tafel slope of 120 mV dec^{-1} was also observed in the higher coverage region of the adsorbed hydrogen atom (θ_H = 0.6) for the determining step of the Heyrovsky rate. Such a Tafel slope value, namely 120 mV dec^{-1}, cannot therefore be due solely to the Volmer step; it must derive either from the Volmer or from the Heyrovsky rate-determining step with high θ_H values.[67] The values of β_c estimated for ZT and ZT* catalysts (125 and 122 mV dec^{-1}), which are close to that of the Pt/C catalyst (119 mV dec^{-1}), refer to efficient HER catalytic performance.

3.2.2 | Electrochemical active surface area (EASA) calculation

Another important parameter used to assesscatalysts' activity is their electrochemical active surface area (EASA), which can be calculated using Eq. (10):[68,69]

$$EASA = C_{dl} / C_s \quad (10)$$

where C_{dl} is the double-layer capacitance of the investigated catalyst, estimated from the CV measurements performed at various potential scan rates, Figure 6 (a-e). The C_s in Eq. (10) refers to the double-layer capacitance of a 1.0 cm^2 flat electrode.

Values of C_{dl} were obtained from the slope of half the difference in current density between anodic and cathodic scans, ($\Delta J = J_{anodic} - J_{cathodic}$)/2, against potential scan rateplots.[70,71] The C_{dl} value calculated for the ZT* catalyst (57.9 mF cm^{-2}) is about 1.5 and 12 times greater than those determined for ZT (39.9 mF cm^{-2}) and Z catalysts (4.74 mF cm^{-2}), and close to Pt/C (64 mF cm^{-2}). The typical value of C_s for such electrodes ranges from 20 to 60 μF cm^{-2}.[70,71] This range of capacitance values gives an average value of 40 μF cm^{-2}. This average value of C_s when inserted in Eq. (10) gives EASA values of 119, 998, and 1498 cm^{-2} for Z, ZT, and ZT* catalysts, respectively. The EASA value of ZT* markedly approached that of the Pt/C (1600 cm^{-2}). These findings refer to the larger accessible active surface area of ZT and ZT* catalysts as compared with Z catalyst, which expedites the electron transport at the electrode-electrolyte interface thus promoting HER kinetics.[72]

3.2.3 | Active sites density and turnover frequency calculations

The number of active sites (n, mol) on catalyst's surface can be calculated from Eq. (11):[73]

$$n = Q_{net}/2F \quad (11)$$

F is the Faraday constant (96485 C / mol), and number 2 corresponds to the number of transmitted electrons during the HER's development. Q_{net} is the catalyst's net voltammetry charge obtained by the

subtraction of charges resulting from GCE (bare surface) from those derived from the tested catalyst, namely the GCE-catalyst electrode: ($Q_{net} = Q_{GCE\text{-}catalyst} - Q_{bare\ GCE}$). Such Q values were derived from catalysts' cyclic voltammograms, Figure 7.

Inserting the obtained Q values (0.001, 0.008, 0.011, and 0.013 C for Z, ZT, ZT* and Pt/C catalysts, respectively) into Eq. (11) gives n values of 5.2×10^{-9}, 4.7×10^{-8}, 6.2×10^{-8}, and 6.7×10^{-8} mol, respectively. The per-site turnover frequencies (TOFs, s^{-1}) can be calculated based on Eq. (12),[73] where I represents the current density (A cm^{-2}) generated at a specified overpotential.

$$\text{TOF} = |I| / 2Fn \quad (12)$$

Consolidating Equations (11) and (12) gives Eq. (13):

$$\text{TOF} = |I| / Q \quad (13)$$

It is, therefore, possible from Eq. (13) to turn the LSV polarization curves' current densities to TOF values, as shown in Figure 8. It follows from Figure 8 that, for any tested catalyst, the TOF value increases with applied potential, where H_2 gas is abundantly evolved. At any applied potential, the value of TOF increases following the sequence: Z < ZT < ZT* ~ Pt/C. For instance, the ZT* catalyst's TOF value at an overpotential of 200 mV is 2.75 s^{-1} per site, which is very close to that estimated for the Pt/C catalyst (2.86 s^{-1} per site), and 4 and 18 times greater than that of ZT (0.7 s^{-1} per site) and Z catalyst (0.15 s^{-1} per site) at the same overpotential. These results support the promising HER catalytic activity of the activated ZT* catalyst, which is comparable to the catalytic performance of the effective HER electrocatalysts in the literature (Supporting Information, Table S3).

3.2.4 | Catalyst activation during long-term stability tests

Figure 9 illustrates ZT catalyst's long-term stability and durability tests using continuous cyclic polarization (CP) for 5,000 and 10,000 cycles and controlled potential electrolysis (CPE) measurements up to 72 h.

A clear enhancement in the cathodic current can be seen after 5,000 and 10,000 cycles, referring to catalyst activation. This increase in the cathodic current enhances with applied cathodic potential where H_2 is liberated progressively, thus revealing the catalytic impact of the evolved H_2.[74] The result of the long-term cathodic polarization test is an activated ZT* catalyst, whose HER activity significantly approached that of the Pt/C catalyst, as shown above. Results of the CPE measurements, chronoamperometry technique conducted at a fixed overpotential, -0.7 V *vs.* RHE (inset of Figure 9), supported CP measurements; the resulting cathodic current is increased throughout the run. These results reveal that the improved HER catalytic activity not only survives as long as the potential (current) is held constant at -0.7 V *vs.* RHE, but also is ameliorated during the operation, a highly promising aspect for the catalyst's practical use over long term operation. Catalyst activation during long-term cathodic processes was a reproducible phenomenon in this work, and formerly obtained in our laboratory.[75-79]

The evolved hydrogen is expected to incorporate into the crystal structure of ZrO_2 NPs creating new defect (catalytically active) sites for the HER.[80] Hydrogen incorporation into the material structure may also break ZrO_2 NPs down due to the hydrogen insertion-induced stress/strain.[80] As a result of this, catalyst surface roughness (i.e., increased ratio of true surface area to apparent surface area) is increased thus, favoring hydrogen generation at reduced overpotentials. CV measurements (revisit Figure 6) supported the enhanced surface area of the catalyst as a result of H_2 insertion. The EASA value of the as-prepared (inactivated) ZT catalyst has markedly increased from 998 cm^2 to 1498 cm^{-2} after cathodic activation (ZT* catalyst).

3.3 | Characterizations of the activated catalyst (ZT*)

Figure 10(a) presents XRD pattern of zirconia powder (ZT* catalyst) obtained after the long-term stability test i.e.72h of chronoamperometry measurements conducted at -0.7 V *vs.* RHE (inset of

Figure 9). Table S4 (Supporting Information) gathers the lattice parameters, collected from profile refinement. In that case, the pattern also exhibited significant peaks broadening, indicating that ZT catalyst maintainedits nanocrystalline nature even after the long-term stability test of the investigated material. ZT* catalyst sample is found to be a single phase as there are no aditional peaks that would correspond to any impurities or secondary phase. The main phase, represented by the Miller indices (hkl), can be assigned to the monoclinic crystal structure of ZrO_2 (*P21/c*, s.g. 14).

The Williamson-Hall plot of $\beta\cos(\theta)$ *versus* $4\sin(\theta)$ for ZT* sample is displayed in Figure 10(b). The crystalline size was estimated from the y-intercept from the linear fit to the data, and the strain from the fit slope. As one can see, for ZT* catalyst sample, the crystallite size and the strain are more than twice larger than for Z and ZT samples.

The XRD observations are further supported by the SEM/EDX and XPS analyses. For XPS studies of ZT* catalyst, the deconvolution model used was analogous to previously presented one (see Figure 11). The stoichiometry of the ZT* catalyst indicates ZrO_2, based on both EDX (Supporting Information, Figure S4) and XPS studies. The monoclinic-to-tetragonal ratio ZrO_2 (M:T), according to the proposed deconvolution model, rises from 2.9 for ZT sample up to 5.7 for ZT*. In this regard, the peak recorded at 182.7 eV for ZT* catalyst should rather be featured as $Zr(OH)_4$, as the XRD revealed no tetragonal structure within these nanoparticles. At the same time, the previously ascribed complex O_{1s} peak at 531.4 eV is significantly smaller for ZT* catalyst, testifying possible removal of the mineralizer during the activation process (ZT* O_{1s} ZrO_2 species share versus other oxygen-containing species is 3.6:1, compared to 1.8:1 for ZT). Due to the removal of the organic species, the third O_{1s} component is primarily explained by the higher capability of ZT* nanoparticles for water chemisorption, consistent with ATR-FTIR and XRD results.

4 | CONCLUSION

In this work, a hydrothermal processing route was adopted to synthesize monoclinic ZrO_2NPs. The process was conducted at 240 °C in the absence and presence of sodium tartrate. Highly dispersible ZrO_2NPs with high amount of disorder were obtained in presence of sodium tartrate, designated as ZT catalyst. ZrO_2 NPs obtained in absence of sodium tartrate were termed as Z catalyst. The catalytic performance of ZT catalyst toward the electrochemical generation of H_2 gas from alkaline solutions significantly exceeded that of the Z catalyst. The high ZT catalyst's HER catalytic performance was attributed, based on XRD examinations, to the abundance of structure defects (and therefore increased number of catalytically active surface sites). Such active sites are rich in surface –OH groups (evidenced from ATR-FTIR spectroscopy studies) and scattered over a large electrochemical active surface area (EASA), as demonstrated from double-layer capacitance (C_{dl}) measurements. It is noticed that, during long-term stability test of ZT catalyst under extreme cathodic conditions, the HER catalytic activity of the ZT catalyst wasmarkedly increased. This long-term cathodic activation process yielded an activated ZT catalyst (designated as ZT* catalyst) with HER catalytic performance approaching that of the commercial Pt/C catalyst. The higher catalytic activity of ZT* nanoparticles may be explained by its altered structure (increased surface area and microstrain), resulting from further hydroxylation (surface –OH groups).The increase of microstrain and Zr-O-H of ZrO_2 nanoparticles after cathodic activation of the catalyst was concluded based on XRD and XPS studies, respectively. Also, increasing the degree of hydroxylation, as expected, opens cavities in zirconia structure, which results in enhanced surface area as determined from double-layer capacitance (C_{dl}) measurements.

ACKNOWLEDGEMENT

This study was funded by the Deanship of Scientific Research, Taif University, Saudi Arabia (Project No.1-439-6068).

ORCID

Mohammed A. Amin: https://orcid.org/0000-0001-7024-8034

REFERENCES

1. Ghosh S, Basu RN. Multifunctional nanostructured electrocatalysts for energy conversion and storage: current status and perspectives. *Nanoscale*.2018;10:11241-11280.

2. Conway BE, Tilak BV. Interfacial Processes Involving Electrocatalytic Evolution and Oxidation of H_2, and the Role of Chemisorbed H. *Electrochim Acta*.2002;47:3571−3594.

3. Durst J, Siebel A, Simon C, Hasche F, Herranz J, Gasteiger HA. New insights into the electrochemical hydrogen oxidation and evolution reaction mechanism. *Energy Environ Sci*. 2014;7:2255–2260

4. Strmcnik D, Uchimura M, Wang C, Subbaraman R, Danilovic N, van der Vliet D, Paulikas AP, Stamenkovic VR, Markovic NM, Improving the hydrogen oxidation reaction rate by promotion of hydroxyl adsorption. *Nature Chem*.2013;5:300 – 306.

5. Sheng W, Zhuang Z, Gao M, Zheng J, Chen JG, Yan Y. Correlating hydrogen oxidation and evolution activity on platinum at different pH with measured hydrogen binding energy. *Nature Commun.*2015;6:5848.

6. Rheinlander PJ, Herranz J, Durst J, Gasteiger HA. Kinetics of the Hydrogen Oxidation/Evolution Reaction on Polycrystalline Platinum in Alkaline Electrolyte Reaction Order with Respect to Hydrogen Pressure. *J Electrochem Soc.* 2014;161:F1448 – F1457.

7. G. Li, J. Yu, Z. Zhou, R. Li, Z. Xiang, Q. Cao, L. Zhao, X. Wang, X. Peng, H. Liu, W. Zhou, N-Doped Mo_2C Nanobelts/Graphene Nanosheets Bonded with Hydroxy Nanocellulose as Flexible and Editable Electrode for Hydrogen Evolution Reaction, iScience.2019;19:1090-1100.

8. Deng Y, Liu Z, Wang A, Sun D. Chen Y, Yang L, Pang J, Li H, Li H, Liu H, Zhiu W. Oxygen-Incorporated MoX (X: S, Se or P) Nanosheets via Universal and Controlled Electrochemical Anodic Activation for Enhanced Hydrogen Evolution Activity. *Nano Energy.* 2019;62:338−347.

9. L. Zeng, L. Yang, J. Lu, J. Jia, J. Yu, Y. Deng, M. Shao, W. Zhou, One-step synthesis of Fe-Ni hydroxide nanosheets derived from bimetallic foam for efficient electrocatalytic oxygen evolution and overall water splitting, *Chin Chem Lett.* 2008;29:1875-1878.

10. Markovica NM, Sarraf ST, Gasteiger HA, Ross PN. Hydrogen Electrochemistry on Platinum Low-Index Single-Crystal Surfaces in Alkaline Solution. *J Chem Soc Faraday Trans.*1996;92:3719−3725.

11. Rheinlander P, Henning S, Herranz J, Gasteiger HA. Comparing Hydrogen Oxidation and Evolution Reaction Kinetics on Polycrystalline Platinum in 0.1 and 1 M KOH. *ECS Trans.*2013;50:2163−2174.

12. Zheng Y, Jiao Y, Vasileff A, QiaoS-Z. The Hydrogen Evolution Reaction in Alkaline Solution: From Theory, Single Crystal Models, to Practical Electrocatalysts. *Angew Chem Int Ed.* 2018;57:7568–7579.

13. Mahmood N, Yao Y, ZhangJ-W, Pan L, Zhang X, ZouJ-J. Electrocatalysts for Hydrogen Evolution in Alkaline Electrolytes: Mechanisms, Challenges, and Prospective Solutions. *Adv Sci.* 2018;5:1700464.

14. Safizadeh F, Ghali E, Houlachi G. Electrocatalysis developments for hydrogen evolution reaction in alkaline solutions: A Review. *Int J Hydrogen Energy*. 2015;40:256–274.

15. Los P, Rami A, Lasia A. Hydrogen evolution reaction on Ni-Al electrodes. *J Appl Electrochem.*1993;23:135 – 140.
16. Lasia A, Handbook of fuel cells: Fundamentals, technology and applications. Vol. 2, Wiley, Chichester, 2003, pp. 416 – 416.
17. Birry L, Lasia A. Studies of the Hydrogen Evolution Reaction on Raney Nickel—Molybdenum Electrodes. *J Appl Electrochem.* 2004;34:735 – 749.
18. Solmaz R, Yüksel H. Fabrication, characterization and application of three-dimensional copper nanodomes as efficient cathodes for hydrogen production. *Int J Hydrogen Energy.* 2019; 44:14108-14116.
19. Yüksel H, Özbay A, Kahraman M, Solmaz R. The effect of 3D silver nanodome size on hydrogen evolution activity in alkaline solution. *Int J Hydrogen Energy*. 2018;43:10586-10594.
20. Taşçı BS, Yüksel H, Solmaz R. Three-dimensional nickel nanodomes: Efficient electrocatalysts for water splitting. *Int J Hydrogen Energy*. 2018;43:10580-10585.
21. Demir DD, Salcı A, Solmaz R. Fabrication of Mo-modified carbon felt as candidate substrate for electrolysis: Optimization of pH, current and metal amount. *Int J Hydrogen Energy*. 2018; 43:10540-10548.
22. Demir DD, Salcı A, Solmaz R. Preparation, characterization and hydrogen production performance of MoPd deposited carbon felt/Mo electrodes. *Int J Hydrogen Energy*. 2018;43:10530-10539.
23. Solmaz R. Gold-supported activated NiZn coatings: hydrogen evolution and corrosion studies. *Int J Energy Res*. 2017;41:1452-1459.
24. Ibrahim MM, Mezni A, Alsawat M, Kumeria T, Alrooqi A, Shaltout AA, Ahmed SI, Boukherroub R, Amin MA, Altalhi T. Crystalline ZnO and ZnO/TiO_2 Nanoparticles Derived from

tert-butyl N-(2 mercaptoethyl)carbamatozinc(II) Chelate: Electrocatalytic Studies for H_2 Generation in Alkaline Electrolytes. *Int J Energy Res*. In Press (2020). https://doi.org/10.1002/er.5410

25. Ibrahim MM, Mezni A, Alsawat M, Kumeria T, Das MR, Alzahly S, Aldalbahi A, Gornicka K, Ryl J, Amin MA, Altalhi T. Enhanced hydrogen evolution reaction on highly stable titania-supported PdO and Eu_2O_3 nanocomposites in a strong alkaline solution. *Int J Energy Res*. 2019;43:5367-5383.

26. Ilanchezhiyan P, Kumar GM, Tamilselvan S, Kang TW, Kim DY. Highly efficient overall water splitting performance of gadolinium-indium-zinc ternary oxide nanostructured electrocatalyst. *Int J Energy Res*. In Press (2020) https://doi.org/10.1002/er.5423.

27. Sun M, Wang Z, Gao B, Wang S, Wang C, Song X, Lin D. Electrocatalytic hydrogen evolution properties of anionic NiS_2-$Ni(OH)_2$ nanosheets produced on the surface of nickel foam. *Int J Energy Res*. 2020;44:4827-4836.

28. Masoodiyeh F, Karimi-Sabet J, Khanchi AR, Mozdianfard MR. Zirconia nanoparticle synthesis in sub and supercritical water - particle morphology and chemical equilibria. *Powder Technol*. 2015;269:461-469.

29. Krause AR, Senturk BS, Garces HF, Dwivedi G, Ortiz AL, Sampath S, Padture NP. $ZrO_2{\cdot}Y_2O_3$ thermal barrier coatings resistant to degradation by molten CMAS: Part I, Optical basicity considerations and processing. *J Am Ceram Soc.* 2014;97:3943-9

30. Behbahani A, Rowshanzamir S, Esmaeilifar A. Hydrothermal synthesis of zirconia nanoparticles from commercial zirconia. *In: Procedia Engineering*. 2012 pp 908-17

31. Li B, Zhang D, Zhang G, Tang Q. Study on preparation of yttria and ceria stabilized Zirconia spherical hollow powder Gongneng Cailiao. *J Funct Mater.*1997;28:518-21.

32. Chang Q, Zhou J, Wang Y, Meng G. Preparation and characterization of unique foamy zirconia single crystals via sol-gel-hydrothermal method. *In: Key Eng Mater.*2010, pp 451-454.
33. Shi G, Zhen Q, Li R, Chen RF, Yan K, Vannier RN. Preparation of agglomeration-free nanosized ZrO_2-HfO_2-Y_2O_3 composite powders Gongneng Cailiao. *J Funct Mater.* 2006;37:1130-1133.
34. Dell'Agli G, Mascolo G. Hydrothermal synthesis of ZrO_2-Y_2O_3 solid solutions at low temperature. *J Eur Ceram Soc.* 2000;20;139-45.
35. Dell'Agli G, Mascolo G. Agglomeration of 3 mol% Y-TZP powders sythesized by hydrothermal treatment. *J Eur Ceram Soc.* 2001;21:29-35.
36. Feng C, Shi E, Guo J, Yan D, Schulze WA. Characterization and fast firing of nanoscale ZrO_2^+ 3 mol% Y_2O_3 ceramic powder prepared by hydrothermal processing. *J Mater Syn. Proc.* 1995;3:31-37.
37. Joo LH, Won GM, Nam KT. Hydrothermal synthesis and mechanical characterization of 3mol%Y_2O_3-ZrO_2 by urea contents. *Korean J Mater Res.* 2011;21;425-31.
38. Hemeda OM, Mostafa NY, Abd Elkader OH, Ahmed MA. Solubility limits in Mnâ€“Mg ferrites system under hydrothermal conditions. *J Mag Mag Mater.* 2014;364:39-46.
39. Mostafa NY, Heiba ZK, Ibrahim MM. Structure and optical properties of ZnO produced from microwave hydrothermal hydrolysis of tris (ethylenediamine) zinc nitrate complex. *J Mol Struct.* 2015;1079:480-485.
40. Mostafa NY, Hessien MM, Shaltout AA. Hydrothermal synthesis and characterizations of Ti substituted Mn-ferrites. *J Alloys Compds.* 2012;529:29-33.
41. Mostafa NY, Shaltout AA, Omar H, Abo-El-Enein SA. Hydrothermal synthesis and characterization of aluminium and sulfate substituted 1.1 nm tobermorites. *J Alloys Compds.* 2009;467:332-337.

42. Mostafa NY, Mahmoud MHH, Heiba ZK. Hydrolysis of $TiOCl_2$ leached and purified from low-grade ilmenite mineral. *Hydrometallurgy*. 2013;139:88-94.

43. Conti HR, Gonzalez ER. Direct Alcohol Fuel Cells, Materials, Performance, Durability and Applications. Ed. Springer Netherlands, 2014.

44. Abdel Hameed RM, Amin RS, El-Khatib KM, Fetohi AE.Influence of Metal Oxides on Platinum Activity towards Methanol Oxidation in H_2SO_4 solution.*ChemPhysChem*. 2016;17:1054-1061.

45. Amin RS, Fetohi AE, AbdelHameed RM, El-Khatib KM. Electrocatalytic activity of Pt–ZrO_2 supported on different carbon materials for methanol oxidation in H_2SO_4 solution. *Int J Hydrogen Energy*. 2016;41:1846-1858.

46. Liu G, Zhang H, Zhong H, Hu J, Xu D, Shao Z.A novel sintering resistant and corrosion resistant Pt_4ZrO_2/C catalyst for high temperature PEMFCs. *Electrochim Acta*. 2006;51:5710–5714.

47. Bai Y, Wu J, Xi J, Wang J, Zhu W, Chen L, Qiu X. Electrochemical oxidation of ethanol on Pt–ZrO_2/C catalyst. *Electrochem Commun*. 2005;7:1087–1090.

48. Cheng N, Banis MN, Liu J, Riese A, Li X, Li R, Ye S, Knights S, Sun X. Extremely Stable Platinum Nanoparticles Encapsulated in a Zirconia Nanocage by Area-Selective Atomic Layer Deposition for the Oxygen Reduction Reaction. *Adv Mater*. 2014;27:277–281.

49. Aguilar-Vallejo A, Álvarez-Contreras L, Guerra-Balcázar M, Ledesma-García J, Arriaga LG, Arjona N, Rivas S. Electrocatalytic Evaluation of Highly Stable Pt/ZrO_2 Electrocatalysts for the Methanol Oxidation Reaction Synthesized Without the Assistance of Any Carbon Support. *ChemElectroChem*. 2019;6:2107-21118.

50. Mostafa NY, Zaki ZI, Mohsen Q, Alotaibi SH, Abd El-moemen A, Amin MA. Carboxylate-assisted synthesis of highly-defected monoclinic zirconia nanoparticles. *J Mol Struct*. 2020;1214:128232.

51. Kouva S, Honkala K, Lefferts L, Kanervo J.Review: monoclinic zirconia, its surface sites and their interaction with carbon monoxide. *Catal Sci Technol.* 2015;5:3473-3490.

52. Williamson GK, Hall WH. X-ray line broadening from filed aluminum and wolfram. *Acta Metall.*1953;1:22-31.

53. Sidhu GK, Kumar R. Role of anionic and cationic surfactants on the structural and dielectric properties of ZrO_2 nanoparticles. *Appl Surf Sci*. 2017;392:598-607.

54. Kouva S, Honkala K, Lefferts L, Kanervo J. Review: Monoclinic zirconia, its surface sites and their interaction with carbon monoxide. *Catal Sci Tech.* 2015;5:3473-3490.

55. Padovini DSS, Pontes DSL, Dalmaschio CJ, Pontes FM, Longo E. Facile synthesis and characterization of ZrO_2 nanoparticles prepared by the AOP/hydrothermal route. *RSC Adv*. 2014;4:38484-38490.

56. Singh A, Nakate UT. Microwave synthesis, characterization, and photoluminescence properties of nanocrystalline zirconia.*Scie World J*. 2014;2014: 1-7.

57. Phillippi C, Mazdiyasni K. Infrared and Raman spectra of zirconia polymorphs. *J Am Ceram Soc.*1971;54:254-258.

58. Lackner P, Zou Z, Mayr S, Diebold U, Schmid M. Using photoelectron spectroscopy to observeoxygen spillover to zirconia. *PhysChemChemPhys.* 2019;21:17613-17620.

59. Cristian D. Miranda M, Alfonso E. Ramírez S, Juradob SG, Vera CR. Superficial effects and catalytic activity of ZrO_2–SO_4^{2-}as a function ofthe crystal structure. *J Mol Cat A: Chemical*. 2015;398:325–335.

60. Ghuang C, Tang Z, Zhang Z. Differences between zirconium hydroxide ($Zr(OH)_4.nH_2O$) and hydrous zirconia ($ZrO_2.nH_2O$). *J Am Ceram Soc.* 2001;84:1637-1638.

61. McEntee M, Peterson GW, Balboa A, Iordanov I, Balow RB, Pehrsson PE. Surface Chemistry of Sulfur Dioxide on $Zr(OH)_4$ Powder: The Role of Water. *J Phys Chem C.* 2019;123:17205-17213.

62. Wysocka J, Cieslik M, Krakowiak S, Ryl J. Carboxylic acids as efficient corrosion inhibitors of aluminium alloys in alkaline media, *Electrochim Acta.* 2018;289:175-192.

63. Luo X, Wang X, Bao S. *et al.* Adsorption of phosphate in water using one-step synthesized zirconium-loaded reduced graphene oxide. *Sci Rep.* 2016;6:39108.

64. Wysocka J, Krakowiak S. Ryl J. Evaluation of citric acid corrosion inhibition efficiency and passivation kinetics for aluminium alloys in alkaline media by means of dynamic impedance monitoring. *Electrochim Acta*. 2017;258:1463-1475.

65. Zheng Y, Jiao Y, Jaroniec M, Qiao SZ. Advancing the Electrochemistry of the Hydrogen-Evolution Reaction through Combining Experiment and Theory. *Angew Chem Int Ed.* 2015;54:52−65.

66. Conway BE, Tilak BV. Interfacial Processes Involving Electrocatalytic Evolution and Oxidation of H_2, and the Role of Chemisorbed H. *Electrochim Acta.* 2002;47:3571−3594.

67. Shinagawa T, Grcia-Esparza AT, Takanabe K. Insight on Tafel slopes from a microkinetic analysis of aqueous electrocatalysis for energy conversion. *Sci Rep.* 2015;5:13801.

68. Ito Y, Cong WT, Fujita T, Tang Z, Chen MW. High catalytic activity of nitrogen and sulfur co doped nanoporous graphene in the hydrogen evolution reaction. *Angew Chem Int Ed.*2015;54:2131–2136.

69. Xie J, Zhang J, Li S, Grote F, Zhang X, Zhang H, Wang R, Lei Y, Pan B, Xie Y. Controllable Disorder Engineering in Oxygen-Incorporated MoS_2 ultrathin Nanosheets for Efficient Hydrogen Evolution. *J Am Chem Soc.* 2013;135:17881–17888.

70. Tang T, Jiang WJ, Niu S, Liu N, Luo H, Chen YY, Jin SF, Gao F, Wan LJ, Hu JS. Electronic and Morphological Dual Modulation of Cobalt Carbonate Hydroxides by Mn Doping toward Highly Efficient and Stable Bifunctional Electrocatalysts for Overall Water Splitting. *J Am Chem Soc*. 2017;139:8320–8328.

71. Amin MA, El-Bagoury N, Mahmoud MHH, Hessien MM, Abd El-Rehim SS, Wysocka J, Ryl J. Catalytic impact of alloyed Al on the corrosion behavior of $Co_{50}Ni_{23}Ga_{26}Al_{1.0}$ magnetic shape memory alloy and catalysis applications for efficient electrochemical H_2 generation. *RSC Adv*. 2017;7:3635 - 3649.

72. Chen J, Yu D, Liao W, Zheng M, Xiao L, Zhu H, Zhang M, Du M, Yao J. WO3−x nanoplates grown on carbon nanofibers for an efficient electrocatalytic hydrogen evolution reaction. *ACS Appl Mater Interfaces*. 2016;8:18132–18139.

73. Liu Y.-R, Shang X, Gao W.-K, Dong B, Chi J.-Q, Li X, Yan K.-L, Chai Y.-M, Liu Y.-Q, Liu C.-G., Ternary CoS_2/MoS_2/RGO Electrocatalyst with CoMoS Phase for Efficient Hydrogen Evolution. *Appl Surf Sci*. 2017;412:138–145.

74. Fan X, Peng Z, Wang J, Ye R, Zhou H, Cuo X. Carbon-based composite as an efficient and stable metal-free electrocatalyst. *Adv Funct Mater*. 2016;26:3621 - 3629.

75. Darabdhara G, Amin MA, Mersal GAM, Ahmed EM, Das MR, Zakaria MB, Malgras V, Alshehri SM, Yamauchi Y, Szunerits S, Boukherroub R. Reduced graphene oxide nanosheets decorated with Au, Pd and Au–Pd bimetallic nanoparticles as highly efficient catalysts for electrochemical hydrogen generation. *J Mater Chem A*.2015;3:20254-20266.

76. Mezni A, Ibrahim MM, El-Kemary M, Shaltout AA, Mostafa NY, Ryl J, Kumeria T, Altalhi T, Amin MA. Cathodically activated Au/TiO_2 nanocomposite synthesized by a new facile

solvothermal method: An efficient electrocatalyst with Pt-like activity for hydrogen generation. *ElectrochimActa*. 2018;290:404-418.

77. Amin MA, Fadlallah SA, Alosaimi GS, Kandemirli F, Saracoglu M, Szunerits S, Boukherroub R. Cathodic activation of titanium-supported gold nanoparticles: An efficient and stable electrocatalyst for the hydrogen evolution reaction. *Int J Hydrogen Energy*. 2016;41:6326-6341.
78. Darabdhara G, Das MR, Amin MA, Mersal GAM, Mostafa NY, Abd El-Rehim SS, Szunerits S, Boukherroub R. Au-Ni alloy nanoparticles supported on reduced graphene oxide as highly efficient electrocatalysts for hydrogen evolution and oxygen reduction reactions. *Int J Hydrogen Energy*. 2018;43:1424-1438.
79. Amin MA, Fadlallah SA, Alosaimi GS, Ahmed EM, Mostafa NY, Roussel P, Szunerits S, Boukherroub R. Room-Temperature Wet Chemical Synthesis of Au NPs/TiH_2/ NanocarvedTi Self-Supported Electrocatalysts for Highly Efficient H_2 Generation. *ACS Appl Mater Interfaces* 2017;9:30115−30126.
80. Lischka M, Groß A. Hydrogen on palladium: a model system for the interaction of atoms and molecules with metal surfaces, Recent Developments in Vacuum Science and Technology. ed. J Dabrowski, 2003, pp. 111–132, ISBN: 81- 7736-118-X and references therein.

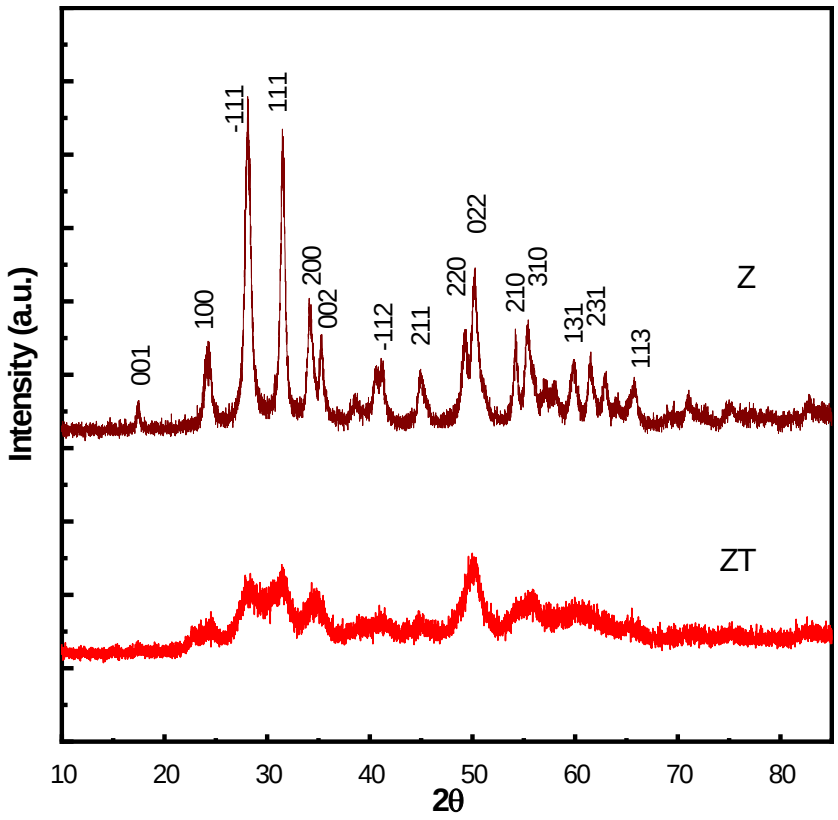

FIGURE 1 XRD patterns of monoclinic zirconia prepared by hydrothermal route: (a) without (Z sample), and (b) with sodium tartrate (ZT sample).

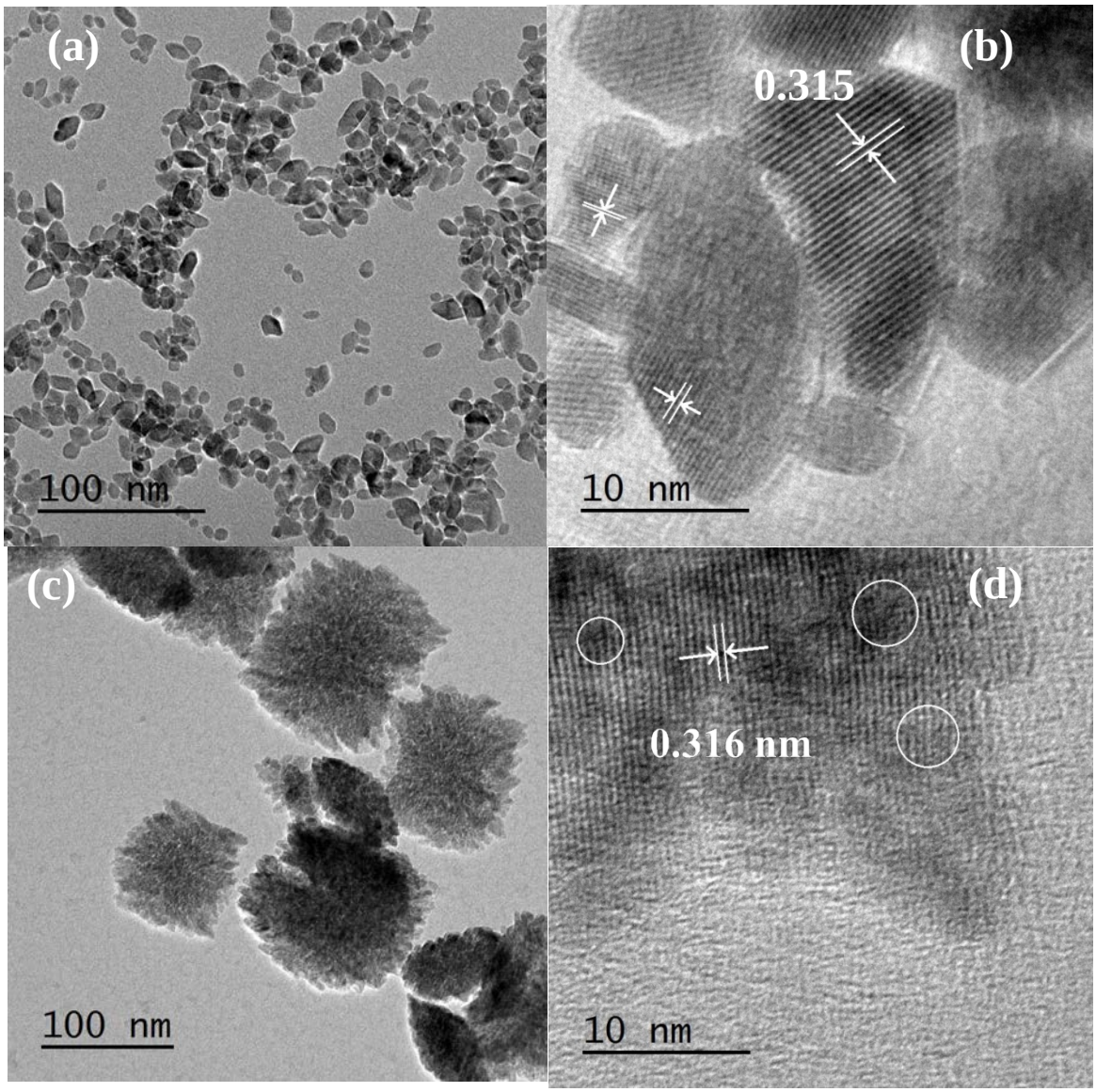

FIGURE 2 TEM and HRTEM images of Z(a,b) and ZT (c,d) samples.

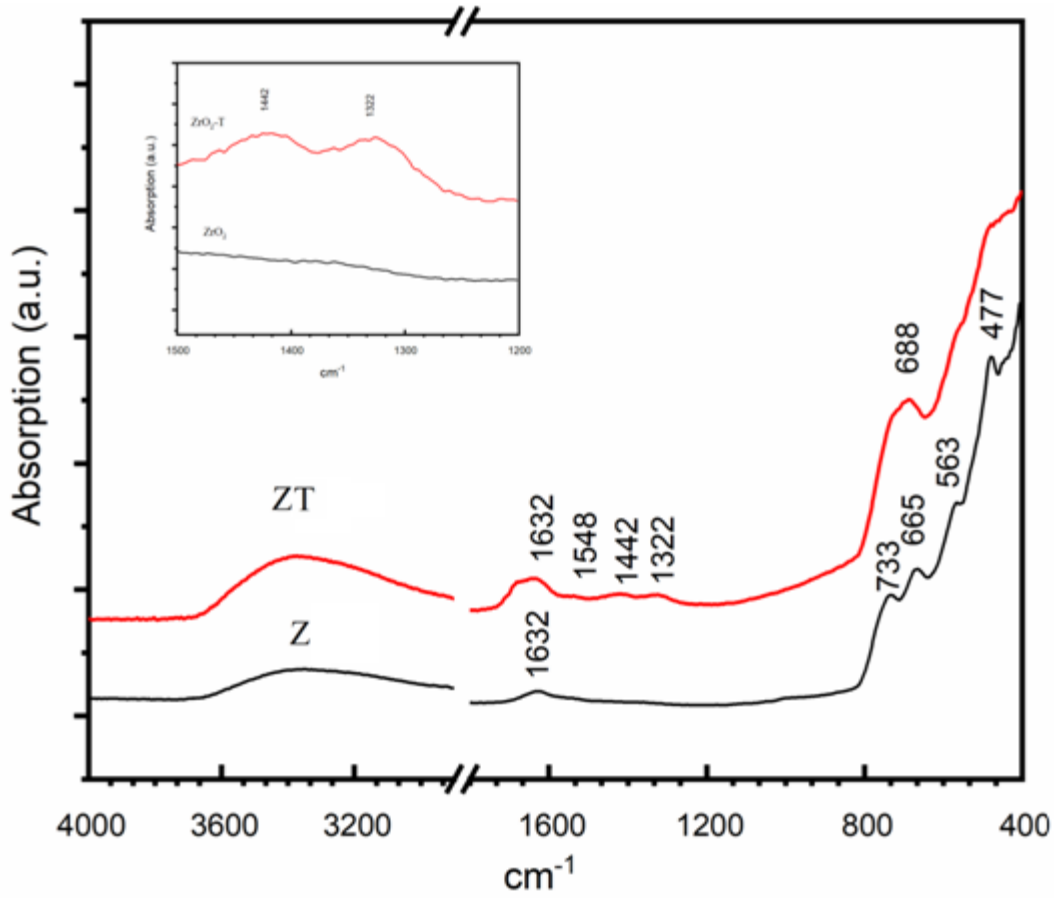

FIGURE 3 ATR-FTIR spectra of the two studied Z and ZT samples.

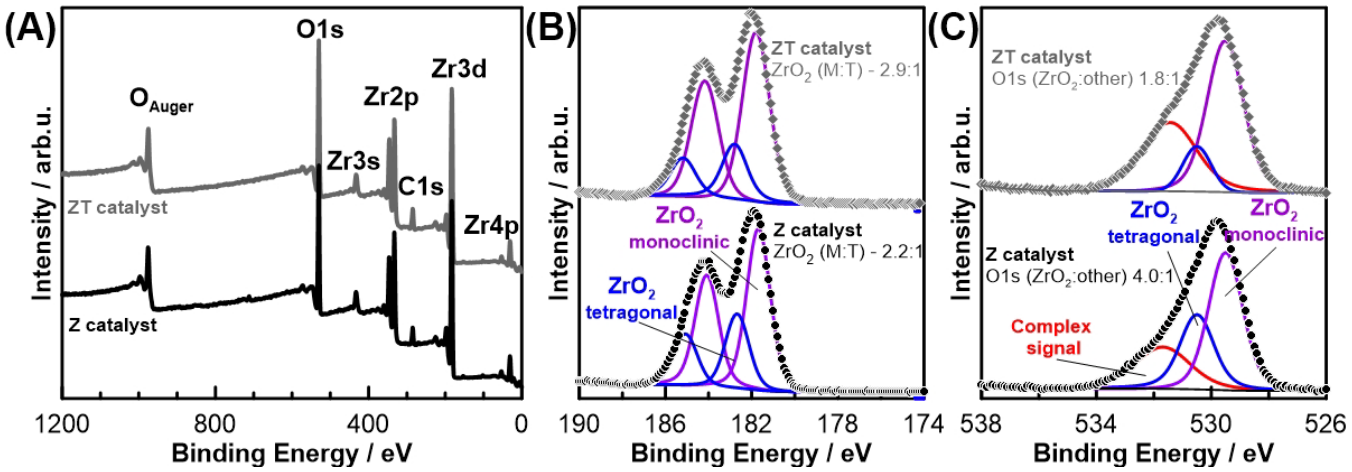

FIGURE 4 XPS analysis of Z and ZT nanoparticles: (A) survey spectra and core level spectra of the Zr_{2p} (B) and O_{1s} (C) with peak deconvolution.

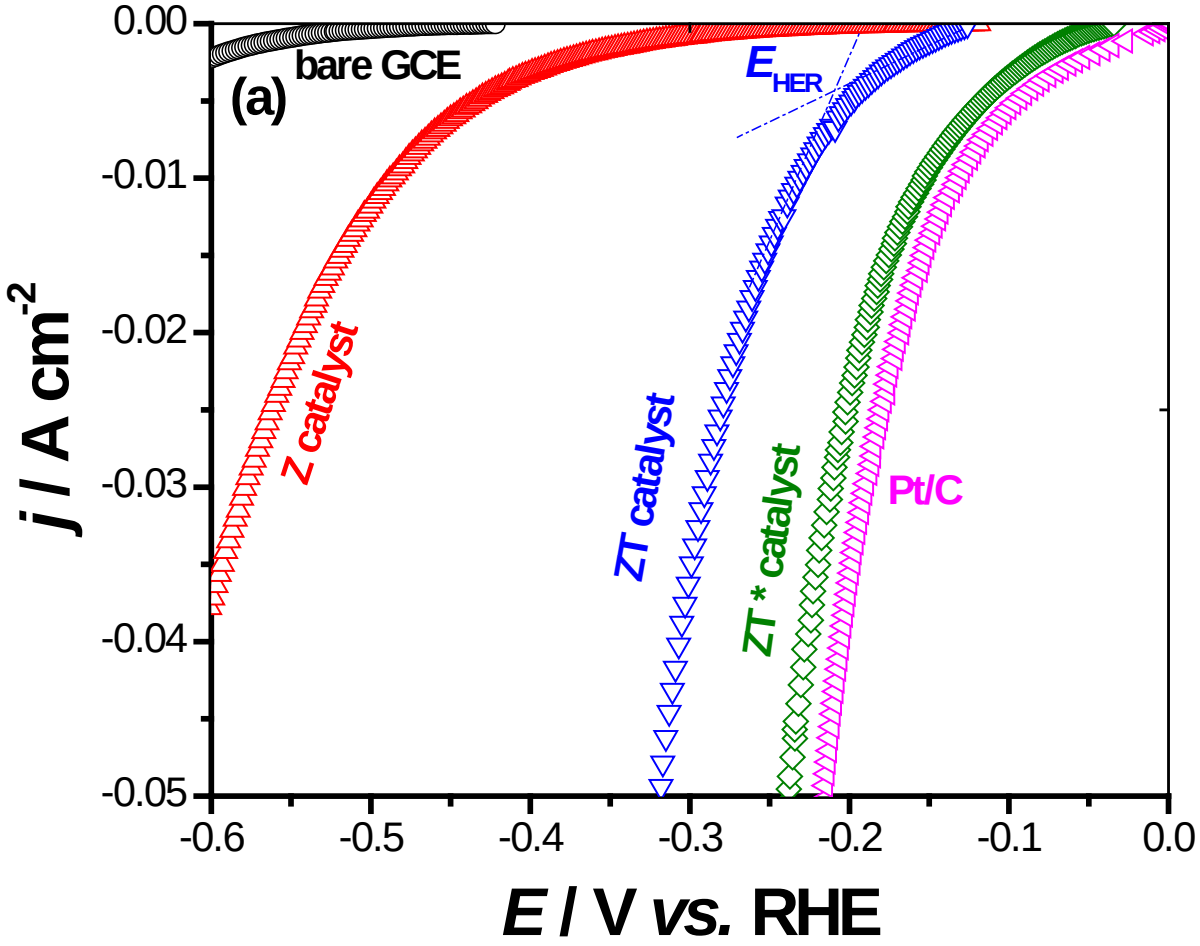

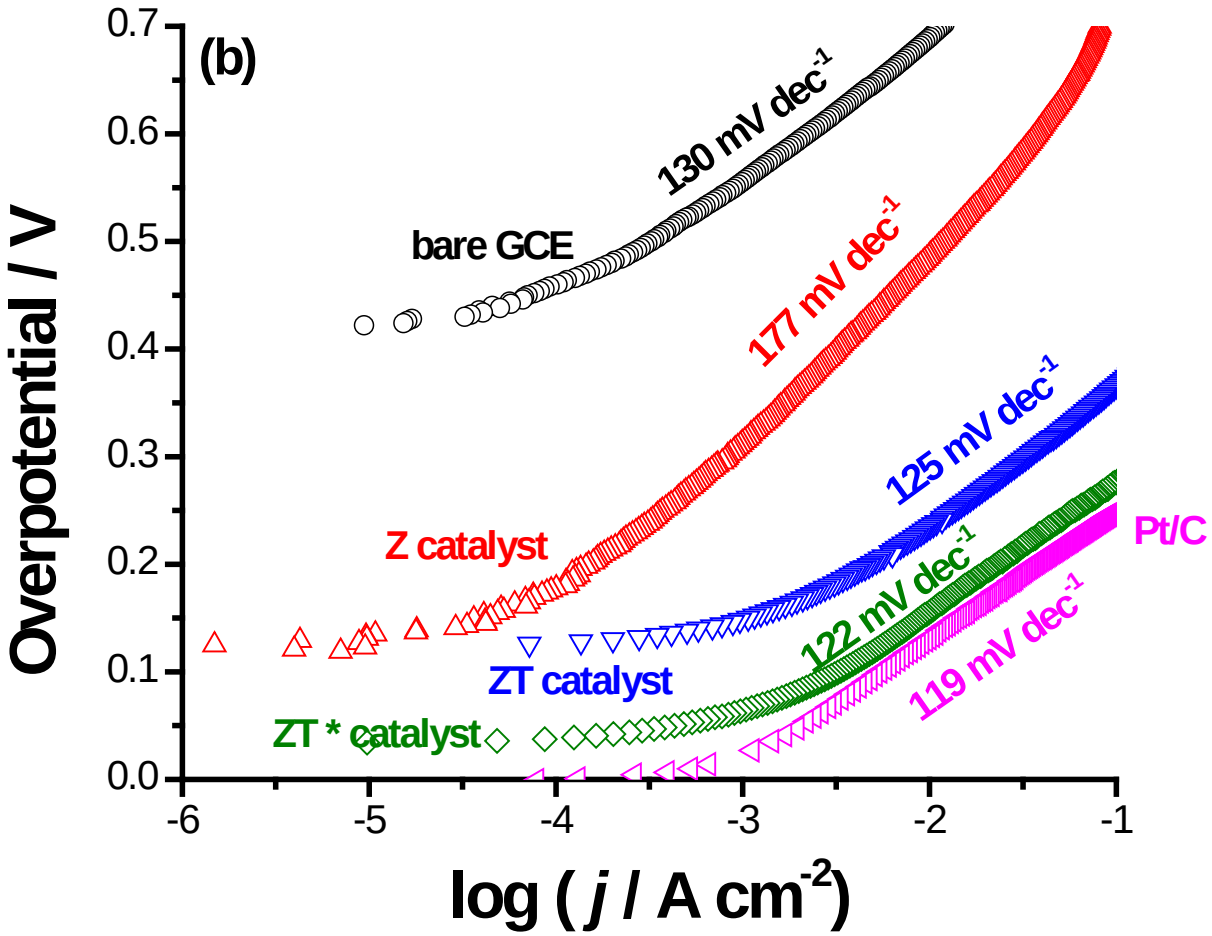

FIGURE 5 Cathodic polarization measurements **(a)** and the corresponding Tafel plots **(b)** recorded for our synthesized catalysts. Measurements were conducted in 1.0 M KOH aqueous solution at a scan rate of 5 mV s^{-1} at room temperature.

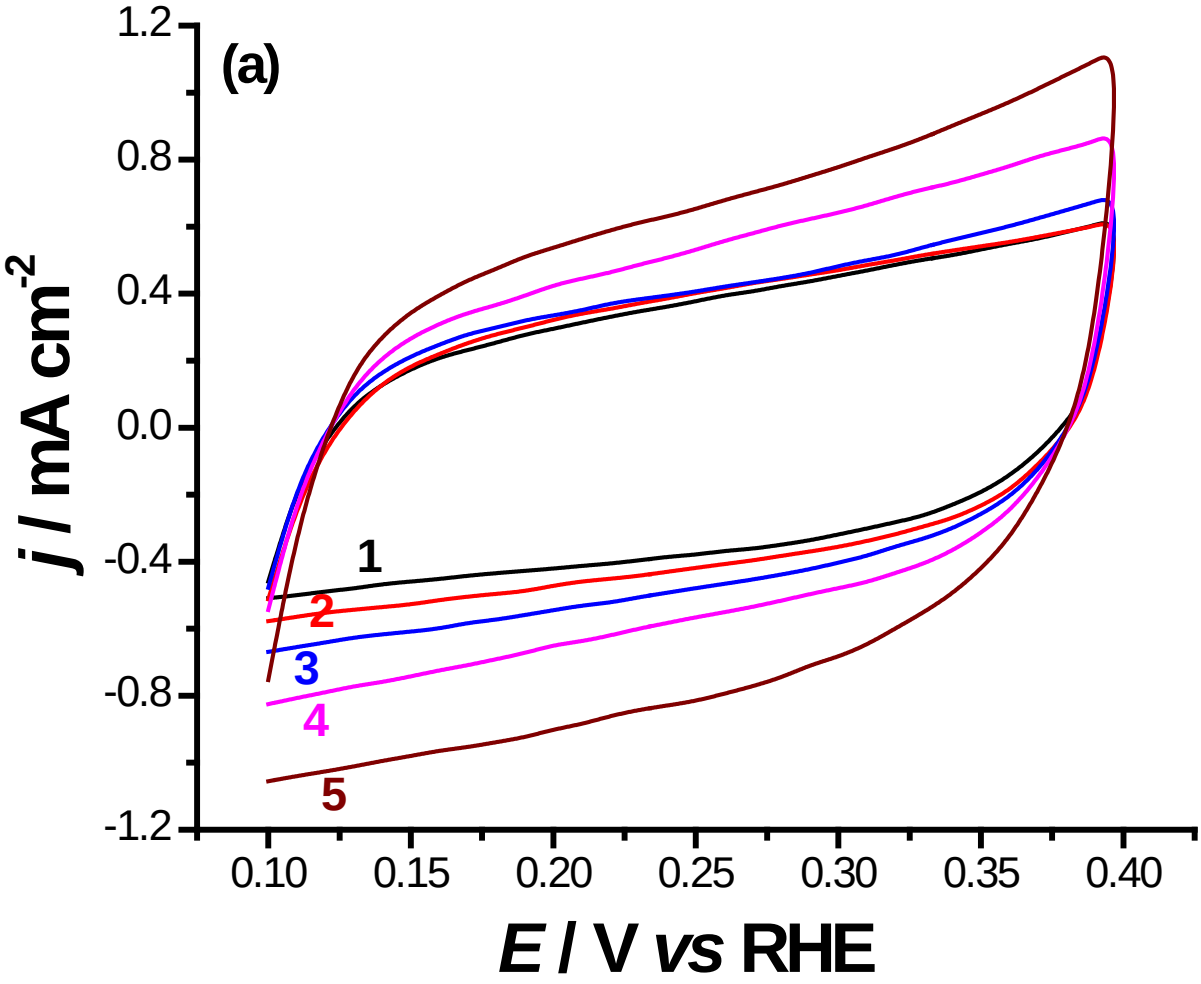

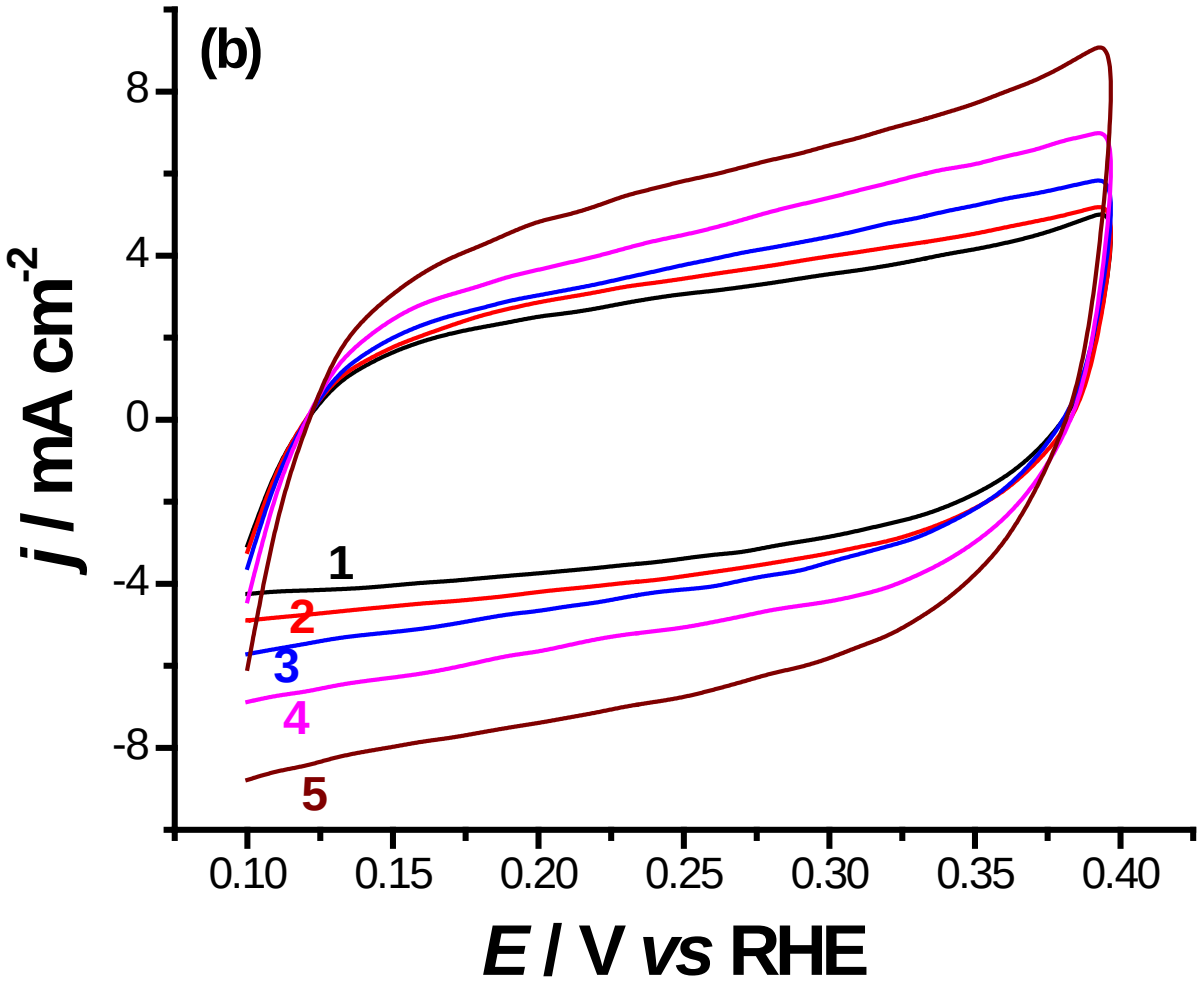

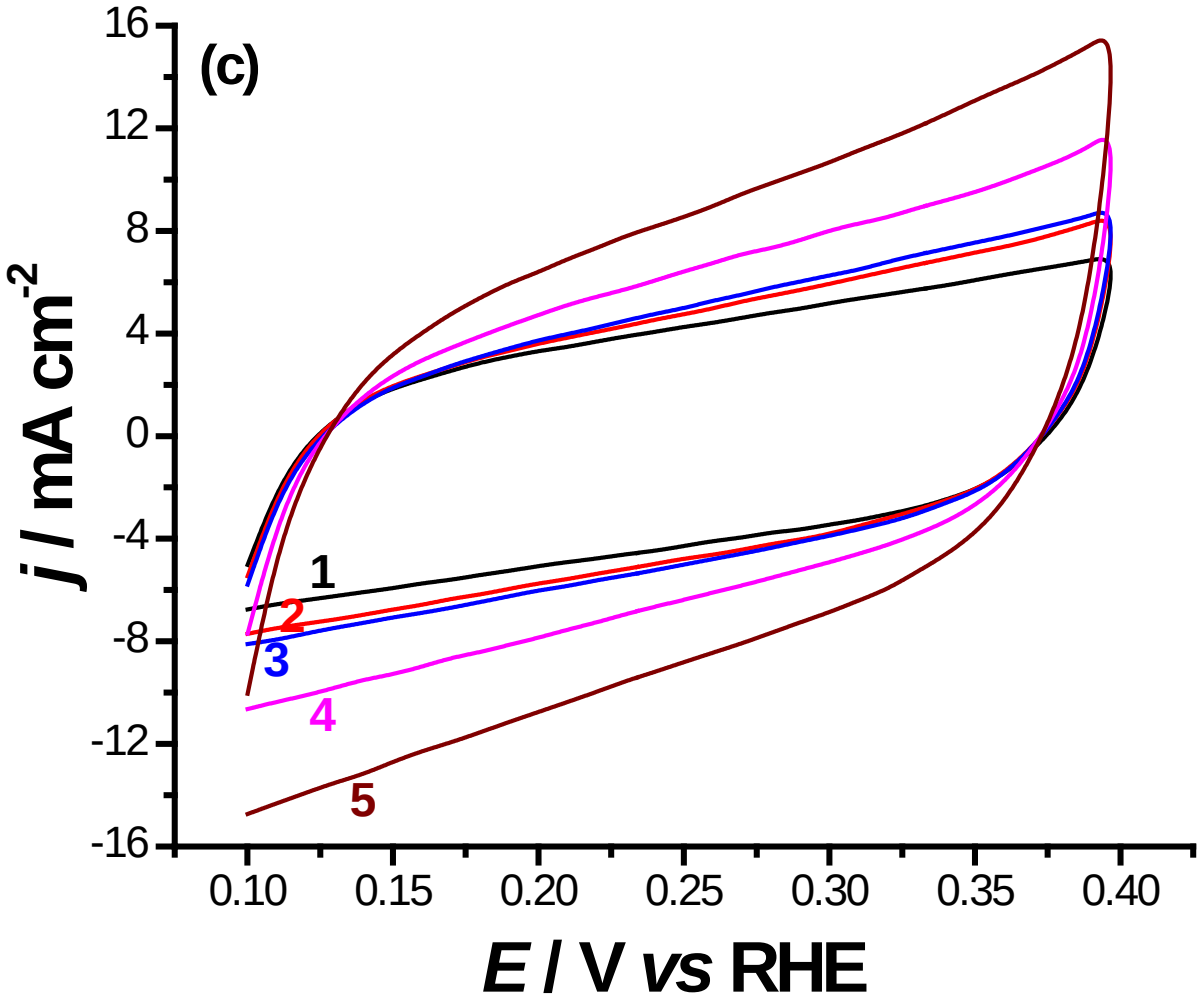

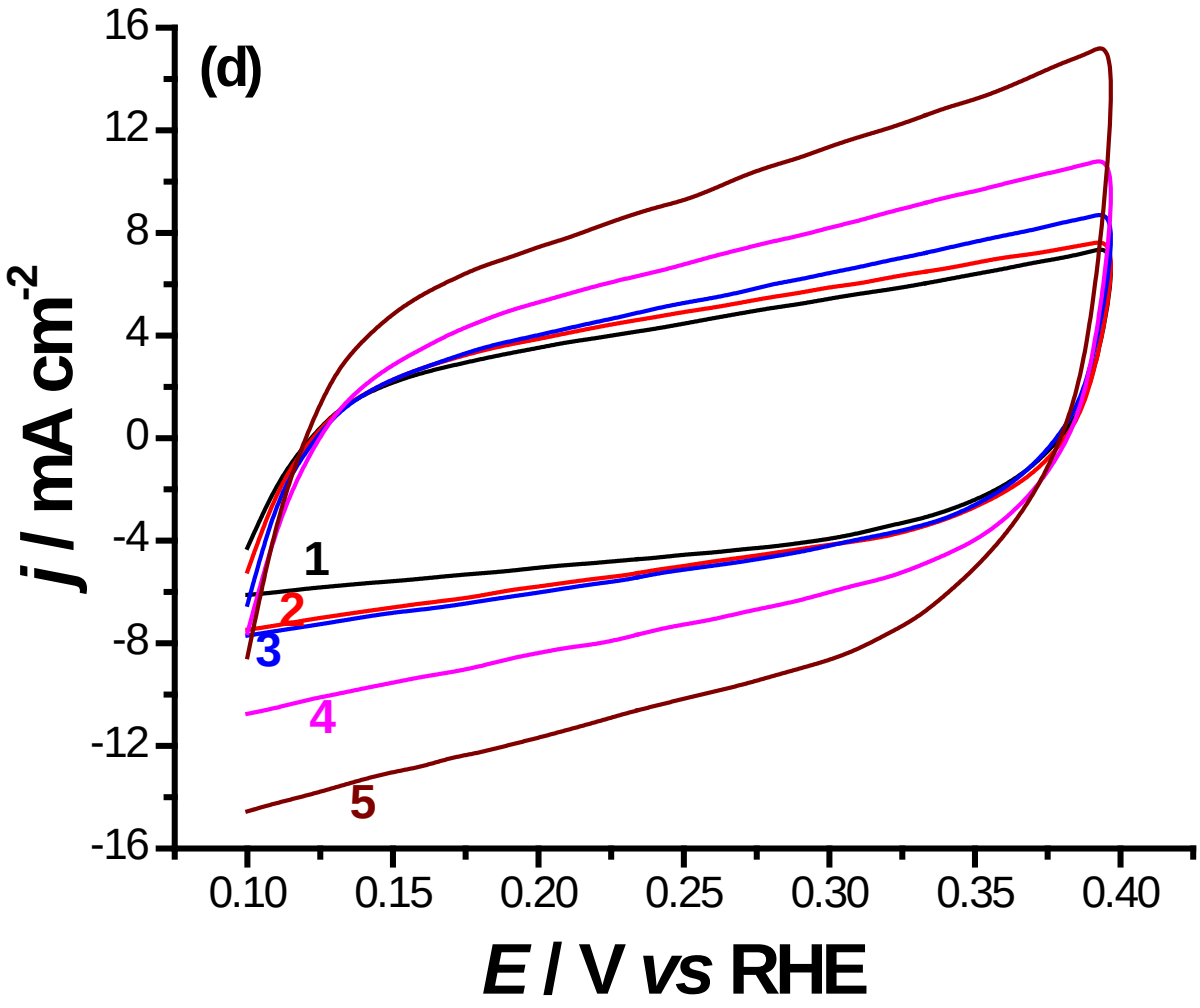

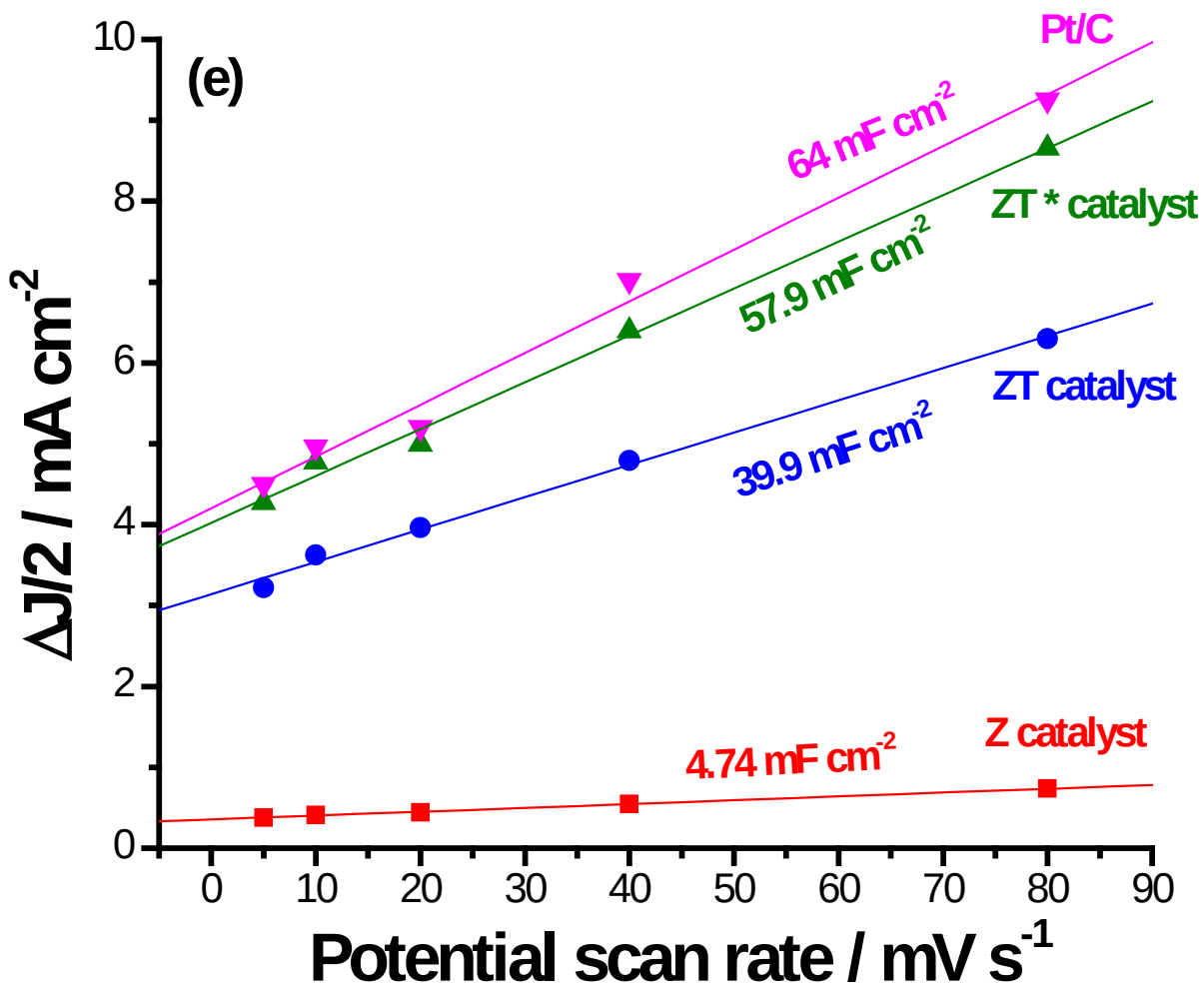

FIGURE 6 CV measurements recorded for Z**(a)**, ZT**(b)**, ZT***(c)**, and Pt/C**(d)** catalysts at various potential scan rates{(1) 5 mV s^{-1}; (2) 10 mV s^{-1}; (3) 20 mV s^{-1}; (4) 40 mV s^{-1}; (5) 80 mV s^{-1}}, and ΔJ/2 *vs.* potential scan rate plots**(e)**. Measurements were conducted in 1.0 M KOH aqueous solution at room temperature.

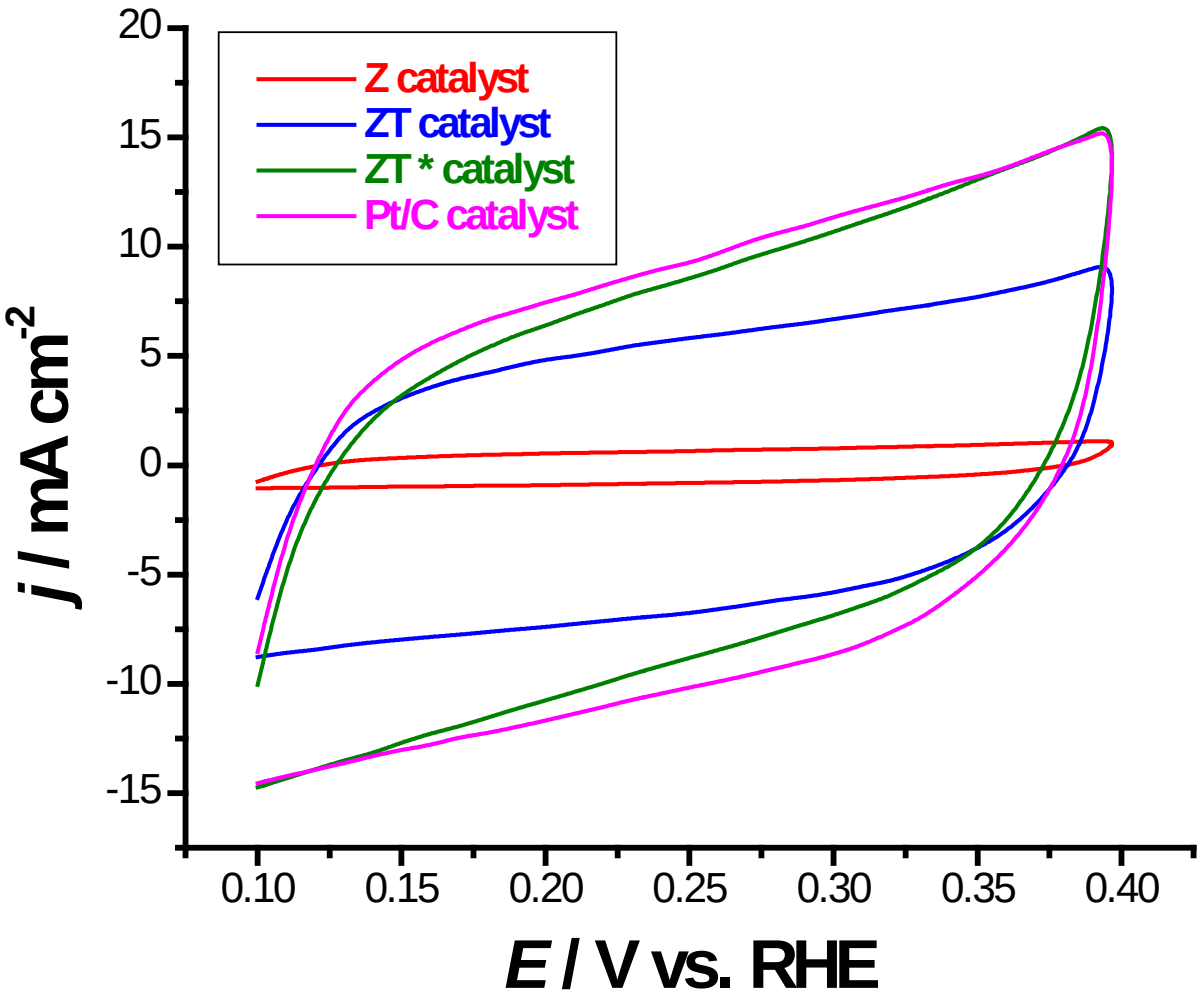

FIGURE 7 CV measurements recorded for Z and ZT catalysts in comparison with Pt/C catalyst. Measurements were conducted in 1.0 M KOH aqueous solution at a scan rate of 80 mV s^{-1} at room temperature.

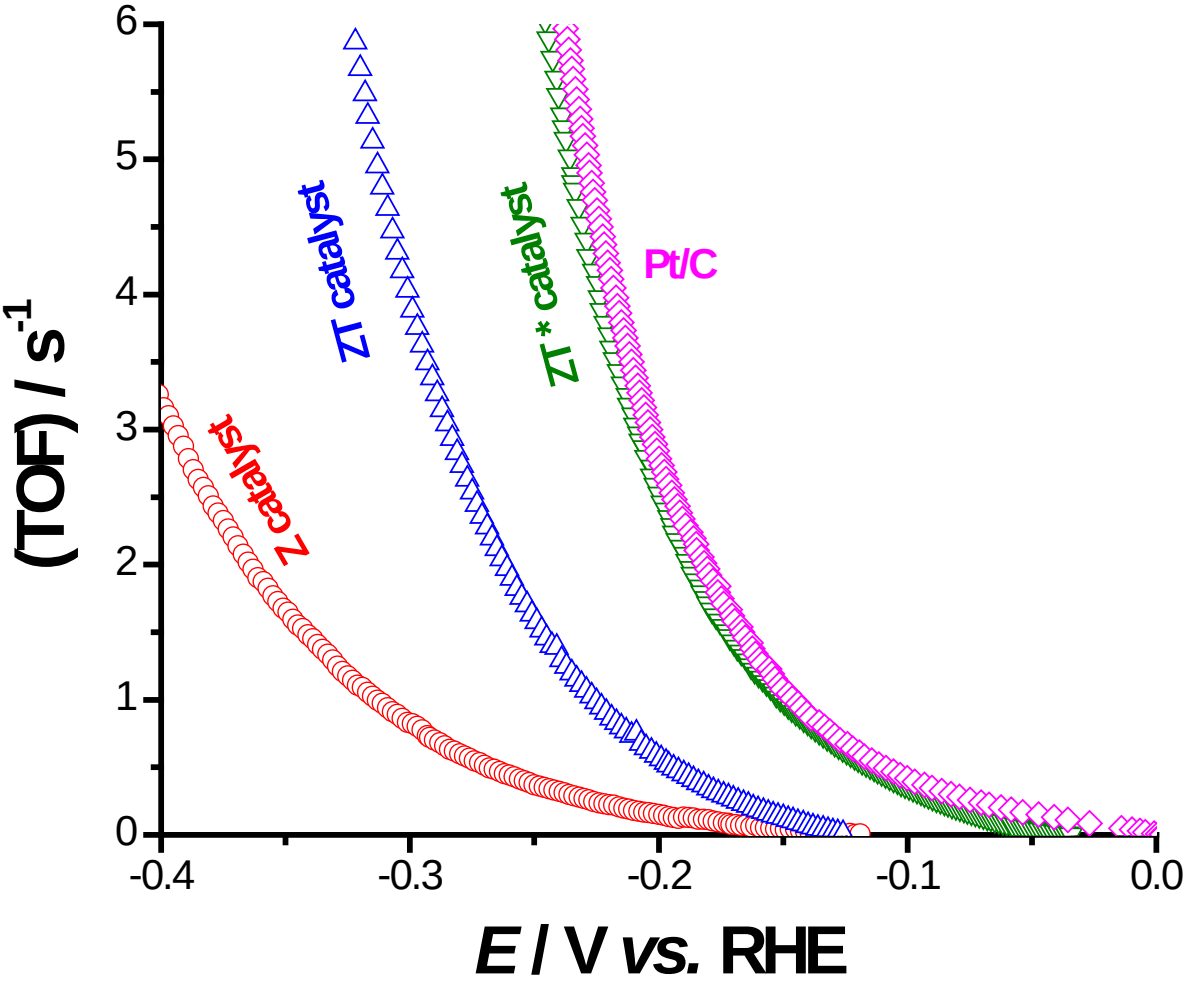

FIGURE 8 The comparison of HER activity normalized by the number of active sites in terms of TOF.

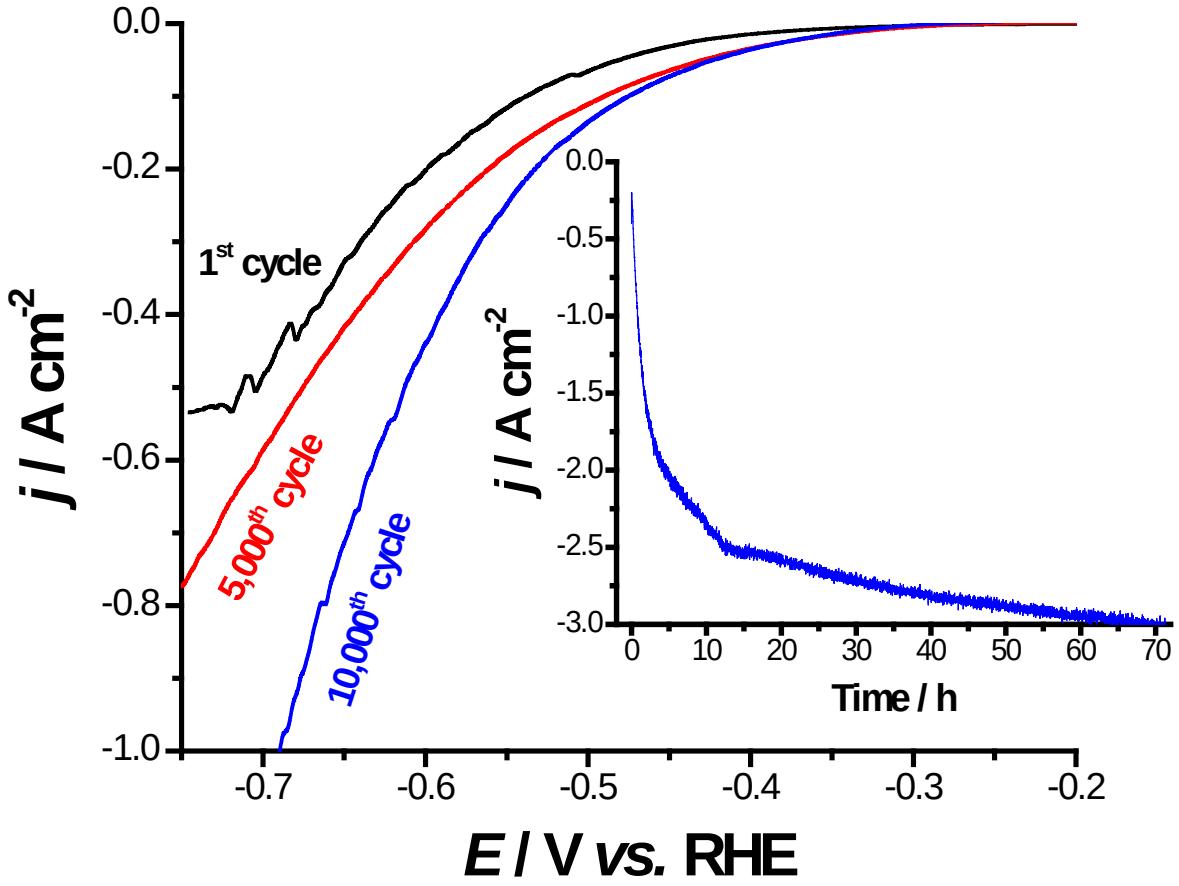

FIGURE 9 Repetitive cycling (5,000 and 10,000 cycles) of the cathodic polarization curves of ZT catalyst. Inset: Chronoamperometry measurements (*j vs. t*) recorded for the catalyst at a constant applied cathodic potential of -0.7 V*vs.*RHE. Measurements were carried out in deaerated KOH aqueous solutions (1.0 M) at 25°C.

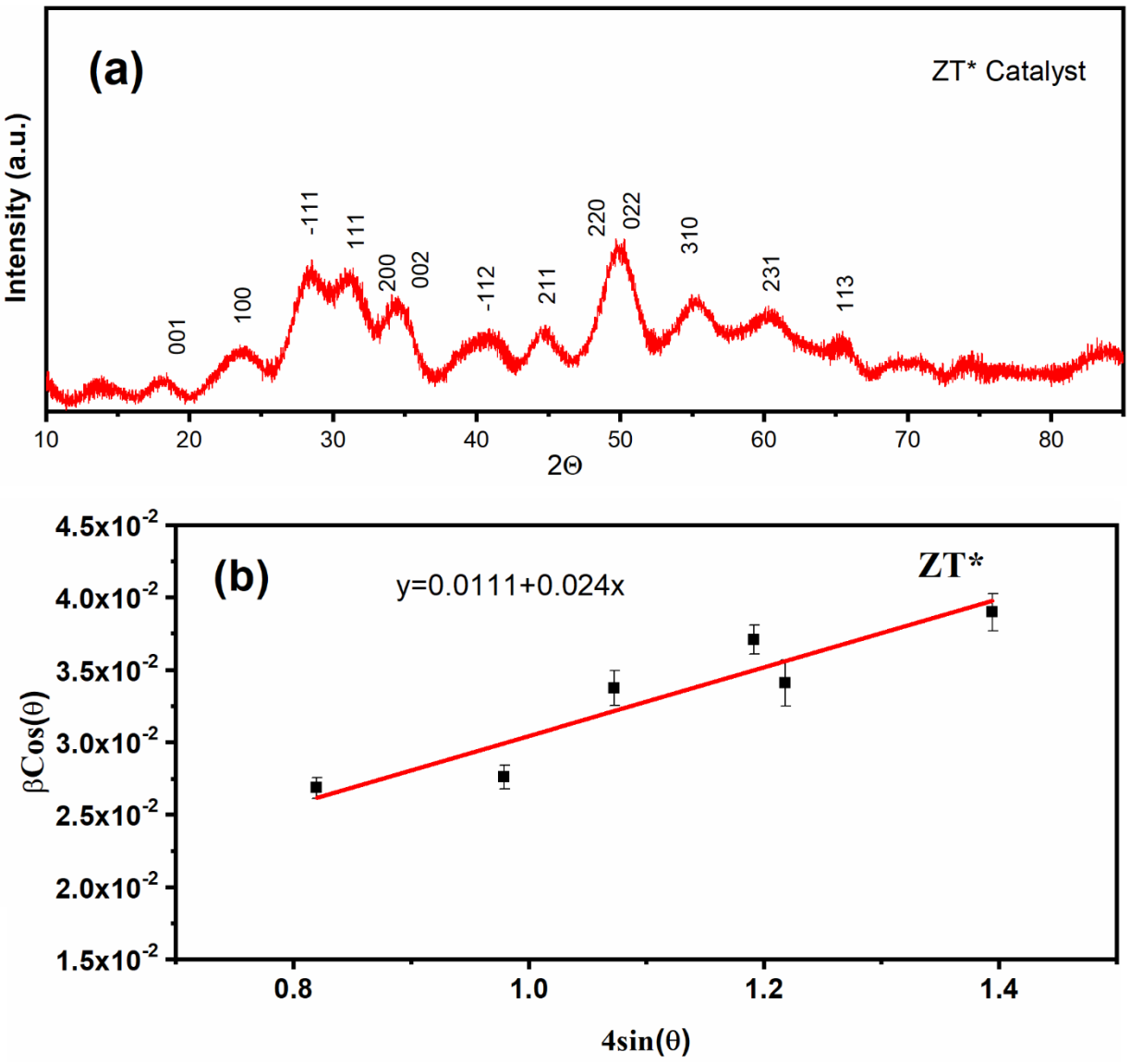

FIGURE 10 (**a**) XRD patterns of zirconia powder prepared by hydrothermal route after cathodic activation (ZT*sample); (**b**) Williamson–Hall plots of ZT* sample.

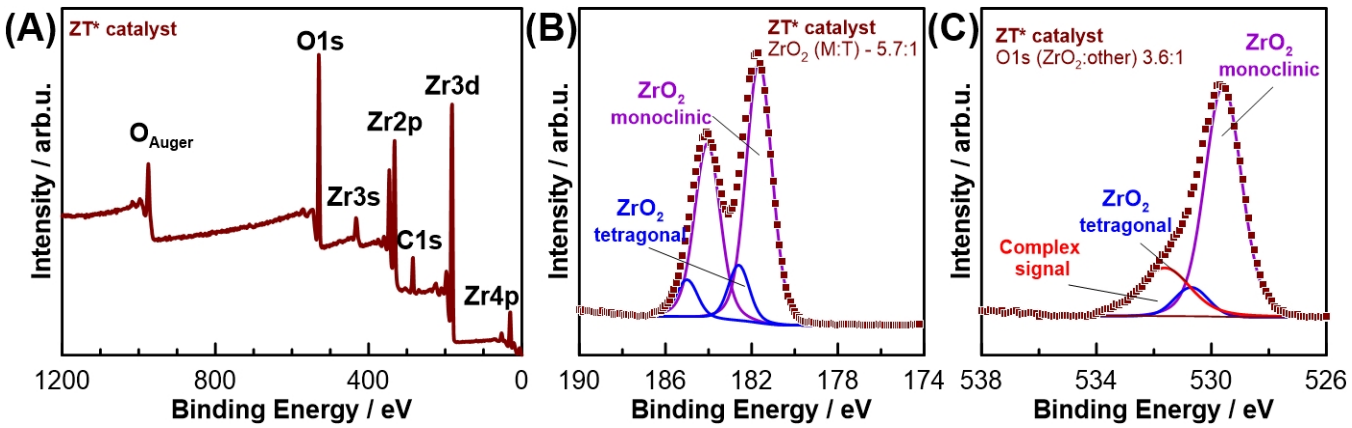

FIGURE 11 XPS analysis of ZT* catalyst: (**A**) survey spectra; high-resolution spectra of the (**B**) Zr_{2p} and (**C**) O_{1s}.

TABLE 1 XPS analysis of investigated Z and ZT catalysts with peak deconvolution.

	ZrO_2monoclinic	$Zr(OH)_4$	ZrO_2monoclinic	$Zr(OH)_4$	C-O bonds / chem. H_2O
BE / eV	181.6	182.7	529.5	530.5	531.4
Z	23.2	10.4	31.7	21.4	13.4
ZT	24.3	8.3	35.2	7.7	24.5

TABLE 2 Mean value (standard deviation) of the electrochemical kinetic parameters for the HER on the surfaces of our synthesized catalysts. Measurements were conducted at room temperature in deaerated KOH solution (1.0 M).

Tested cathode	E_{HER} / mV vs. RHE	Tafel slope ($-\beta_c$, mV dec^{-1})	Exchange current density (j_o, mA cm^{-2})	Overpotential at j = 10 mA cm^{-2} (η_{10} / mV vs RHE)
bare GCE	------	130(1.5)	$3.98(0.05) \times 10^{-5}$	690(7.2)
Z catalyst	-450(4.9)	177(2.1)	$1.8(0.02) \times 10^{-2}$	490(5.0)
ZT catalyst	-202(2.5)	125(1.4)	$2.2(0.03) \times 10^{-1}$	235(2.7)
ZT* catalyst	-88(1.6)	122(1.4)	$4.7(0.06) \times 10^{-1}$	140(1.5)
Pt/C	-55(1.2)	119(1.1)	$6.6(0.05) \times 10^{-1}$	128(1.3)